# INVESTIGATION OF SATURABLE OPTICAL RECEIVER (SOR) FOR FIBER TO THE HOME NETWORK

# INVESTIGATION OF SATURABLE OPTICAL RECEIVER (SOR) FOR FIBER TO THE HOME NETWORK

By

Ning Luo. B.ENG.

A Thesis

Submitted to the School of Graduate Studies

in Partial Fulfillment of the Requirements

for the Degree

Master of Science

McMaster University

MASTER OF APPLIED SCIENCE (2008) McMaster University
Electrical and Computer Engineering Hamilton, Ontario

TITLE: Investigation of Saturable Optical Receiver (SOR) for Fiber to the Home network

AUTHOR: Ning Luo, B.ENG. (McMaster University)

SUPERVISOR: Professor Xun. Li

NUMBER OF PAGES: xii, 105

# Abstract

Due to the high cost, telephone and cable television companies can only justify installing fiber optica lnetworks to remote sites which serve up to a few hundred customers. For customers located at variable distances from the transmitting station, they will receive signals at different strengths.. The signal stability and system reliability of FTTH network affected largely by the distance. We propose an effective solution for the enhancement of signal stability of FTTH network, which uses a semiconductor optical amplifier (SOA) coupled with an optical receiver.

Before the signal reaches the optical receiver at the user end, signal strength is automatically adjusted through a semiconductor optical amplifier (SOA). Due to the special saturation property of SOA, the output optical signal will have very small fluctuation regardless the input optical signal power, the signal stability of FTTH network will be improved significantly. A set of simplified governing equations of SOA has been proposed and the corresponding numerical solver has been implemented. Although the main focus is primarily the SOA, a simplified optical receiver is also simulated, which comprises a PIN photodetector and a low pass filter (LPF). All simulations have been carried out in the time-domain with the frequency domain low pass filter modeled by a digital filter.

## Acknowledgements

I would first like to express my gratitude to my supervisor, Dr. Xun. Li, for cultivating my interest in the area of optical fiber communication, whom I took ECE 755 in my Electrical program. My interaction with him generated a fundamental role in the development of this thesis.

I also want to thank Dr. Shiva Kumar for teaching me Lightwave Communication Systems, and help in suggesting techniques in developing optical receiver of communication system.

Last, but certainly not the least, I would like to thank my family. Constant love and support from my parents have always given me the confidence and drive to pursue and realize my dreams.

# Table of Contents

# List of Figures

# List of Tables

# Chapter 1 Introduction

The basic idea of FTTH is based on transmitting information from a central station to the each individual home by sending light through an optical fiber. On account of many advantages over traditional electrical-based communication, FTTH communication will keep on being a promising technology as an ultimate solution for local broadband access network [1].

## 1.1 Motivation

Depending on the location of the fiber termination point, the fiber access network is often referred to as the fiber-to-the-x (FTTx), where x stands for the location of the fiber termination, e.g., H for home, C for curb, B for building, and N for node, etc [2]. The major difficulties for FTTH technology becoming widely distributed are related to the high cost of construction, and low signal stability at optical network terminal (ONT) [3]. Fiber-to-the-curb (FTTC) and other approaches appeared on the scene to resolve the high cost issue by bringing fiber partway to the home, and serve multiple customers (thus sharing costs) by connecting to each customer through metallic media [1]. FTTH networks have primarily been installed in the densely populated areas, where they can be used to their full transmission capacity. For suburb areas, FTTH networks are more expensive and less effective compared to the copper wires based electrical systems. Theoretically, the signal strength is reversely proportional to the transmitting distance, and signal stability in the FTTH networks has been largely limited by this barrier. In our paper, an effective solution has been proposed to overcome low signal stability issue at optical network terminal (ONT) for each

subscriber, which makes FTTH network more appealing in term of management flexibility and scalability. .

## 1.2 Literature Review

Optical transmitters are the key elements used at communication terminals for converting electrical currents into optical signals, which then sent into optical fibers. Commonly used optical transmitters are semiconductor devices such as light-emitting diodes and laser diodes. Light-emitting diodes use spontaneous emission to generate optical signals, and are very inefficient [5]. Only around 1% of generated optical power can be coupled into the optical fiber [5]. Laser diode uses stimulated emission to generate optical signals, and is very efficient. If the laser diode is designed properly with optimal operating frequency, more than 90% of the generated optical power can be coupled into the fiber [5].

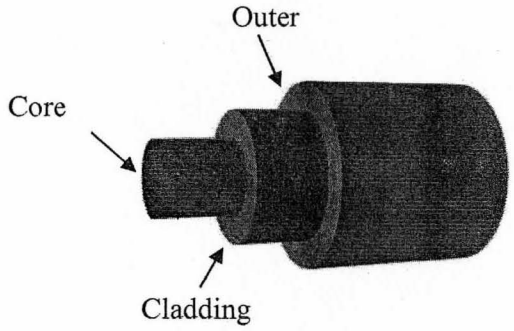


Figure 1-1: A schematic diagram of an optical fiber.

Optical fiber is the only medium capable of moving data at multigigabit-per-second speeds [1]. It consists of a core, cladding, and a protective outer coating. This is shown in the Figure 1-1. In the construction of most fibers, the core and cladding

are made of high-quality silicon glasses or plastics [4]. Two classifications of optical fibers are the multi-mode fiber and single-mode fiber both used in the field of communications. On account of lower attenuation and interference compared to the electrical transmissions, optical fiber has many advantages in long-distance and high-capacity applications. The detailed discussion of optical fiber will be given in Chapter 5.

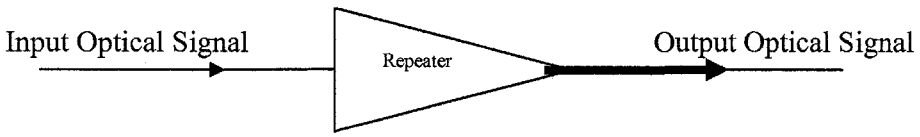


Figure 1-2: A schematic diagram of optical repeater.

Optical fiber is not the only component in the FTTH network; other devices are also involved in the system's operation. During the early development of fiber-optic communication system, the limited transmission distance due to attenuation and distortion of the fiber was the initial hurdle that had to be overcome. The solution thus far has been to use optoelectronic repeaters or an optical amplifier. During the transmission in the fiber, repeaters (amplifiers) will be placed at certain intervals, to prevent the degradation due to range of a signal's strength [4]. This is shown in Figure 1-2. The optoelectronic repeaters do not only simply repeat the signal, but also act as a transmitter. During the repeating process, the optical signal switches back to the electrical domain first, is amplified, and then is sent out again [6]. An alternative approach is to use optical amplifiers. In an optical amplifier, the signals are amplified directly without switching back to the electrical domain [6]. Due to the lower cost and

inherently being less complex, amplifiers have largely replaced repeaters in new fiber-optic communication systems.

When the optical signal reaches the user end of the system, a semiconductor-based photodetector converts the optical signal back into an electrical current through the photoelectric effect [7]. In our paper, the PIN photodetector has been chosen for this purpose. After the signal gets converted to electronic domain, it has to pass through a low pass filter which rids it of high frequency noise. Additional signal processing, such as clock recovery by a phase-locked loop may also be applied [5].

In our paper, we proposed a simplified version of saturable optical receiver (SOR) for the end user's premise, which includes a saturable semiconductor optical amplifier (SOA), a PIN photodetector, and a low pass filter (LPF). We also assumed that the optical fiber is ideal, so that a lossless transmission medium for the optical signal can be assumed

## 1.3 Thesis Organization

We first developed the necessary background theory in Chapter 1. The performance of the SOAs has been investigated systematically through extensive numerical simulation based on the comprehensive broad-band time-domain traveling wave model in Chapter 2. Chapter 3 presents detailed model analysis, and simulations for the PIN photodetector. Detailed DSP realization method of LPF is presented in Chapter 4. Detailed saturable optical receiver (SOR) modeling method and related simulations are presented in Chapter 5. Chapter 6 concludes this work, and provides information on intended future work related to this topic.

## 1.4 Contribution

We proposed an effective solution for the enhancement of signal stability of FTTH network, which uses a semiconductor optical amplifier (SOA) coupled with an optical receiver. A set of simplified governing equations of SOA has been proposed and the corresponding numerical solver has been implemented.

# Chapter 2 Modeling of Semiconductor Optical Amplifier

The large expansion of the telecommunication market requires more organized and flexible evolution of the network infrastructures. The realization of a new generation of optical networks able to manage high-speed data flows is therefore needed [9], [10]. Optical amplifiers provide a possible solution for high-speed optical networks [27]. The purpose of our study is to find the SOA gain dependence on various device parameters. As such we can design a SOA structure with a highly saturated gain to serve for our purpose.

## 2.1 Review of Semiconductor Optical Amplifier

Optical amplifiers can be divided into two classes: optical fiber amplifiers (OFA) and semiconductor optical amplifiers (SOAs) [12]. The former has tended to dominate conventional system applications such as in-line amplification used to compensate for fiber losses; however, due to advances in optical semiconductor fabrication techniques and device design, the SOA is showing great promise for use in evolving optical communication networks [12]. In now days, semiconductor optical amplifiers (SOAs) are one of the most important active components for fiber-optic communication systems and a range of other applications [13]. As optoelectronic integrated circuit technology advances and manufacturing casts fall, the use of SOAs as basic amplifiers and as components in functional subsystems will be greatly expanded [12].

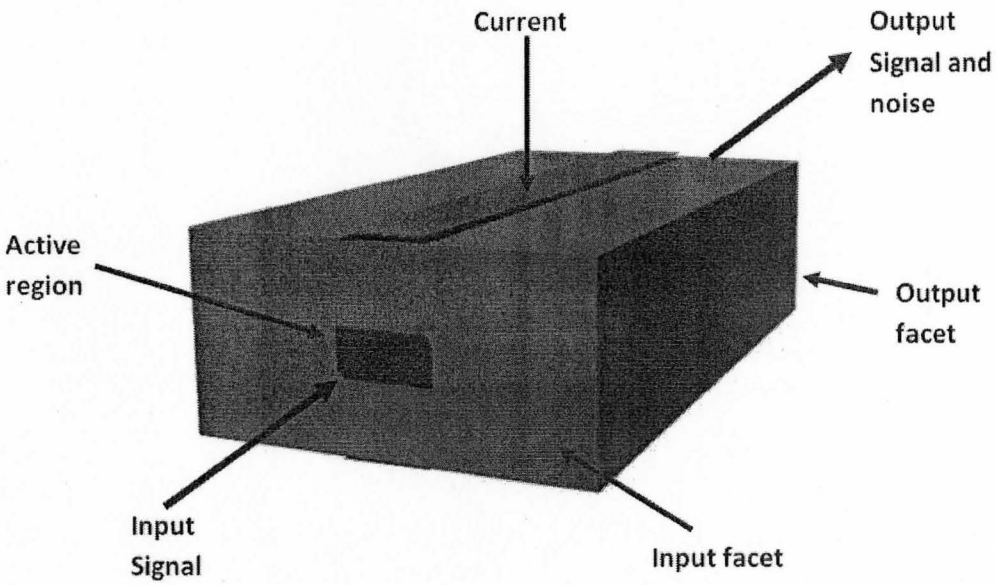


Figure 2-1: Schematic view of a semiconductor optical amplifier (SOA).

The structure of SOA is almost identical to that of the semiconductor laser except for a special designed cavity with polarization-independent gain and antireflection (AR) coated endfaces [11]. The active region in the device imparts gain, via stimulated emission, to an input signal [12]. The output signal is accompanied by noise. This additive noise is produced by the amplified spontaneous emission (ASE) process [12]. The SOA is driven by an injection current, and the gain of SOA is influenced by the input signal power and internal noise generated by the amplification process [12]. As the power of output optical signal increases, the gain decreases. The saturation will occur if the output optical signal power is too high. This is shown in the Figure 2-2.

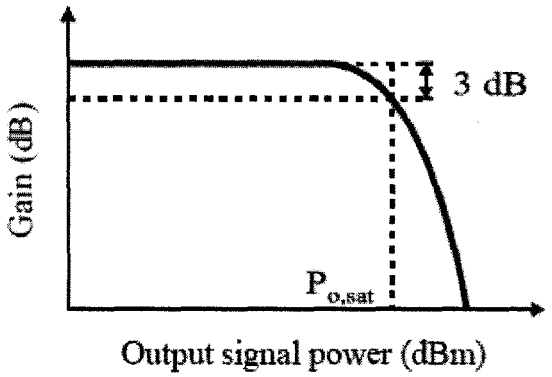


Figure 2-2: Typical SOA gain versus output signal power.

As a stand-alone device, SOA can be used as the replacement of erbium-doped fiber amplifiers (EDFAs) for linear amplifications [20]. The principal applications of SOAs in optical communication systems can be classified into three areas: (a) post-amplifier or booster amplifier to increase transmitter laser power, (b) in-line amplifier to compensate for fiber and other transmission losses in medium and long-haul links and (c) preamplifier to improve receiver sensitivity [12]. SOA can also be utilized as the optical components for nonlinear applications such as wavelength conversion and optical switch [14]. In our paper, we treated SOAs linearly as receiver pre-amplifiers.

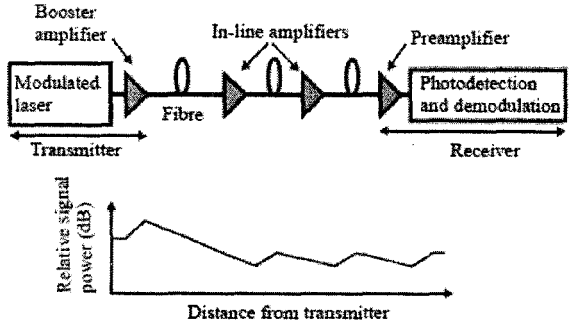


Figure 2-3: Application of SOAs as booster amplifier, in-line amplifiers and preamplifier in an optical transmission link.

The main advantages of SOA are low cost and photonic integration with most optoelectronic components and large amplification bandwidth. The bandwidth if InGaAsP based SOAs extends from 1200nm to 1650nm. The amplification bandwidth of SOAs is quite large, compared to only a 40nm amplification bandwidth from regular EDFAs [8]. The problem with an SOAs is the short lifetime of its electron carriers, about several hundreds of pico-seconds [11]. This short lifetime causes several nonlinear effects in SOA applications: cross gain modulation (XGM), cross phase modulation (XPM) and four-wave mixing (FWM) which will cause interchannel cross-talk and intersymbol interference (ISI) [11]. A strong signal at one wavelength will modulate the gain for another wavelength, because the short lifetime of carriers makes the gain response fast [11]. Some techniques have been developed to minimize the ISI in WDM systems [15].

## 2.2 Modeling of Semiconductor Optical Amplifier

The theoretical foundation for semiconductor optical amplifiers (SOA) modeling was established in 1980s [16], [17]. Since then major progress on semiconductor optical amplifier modeling focuses on the material gain coefficient, spontaneous emission rate and the fraction of spontaneous emissions coupled into the guided waves in an amplifier [11]. Some numerical simulations using the Finite Difference Method (FDM) have been studied intensively to solve carrier rate equation and traveling wave equations [11]. In parallel, some simplified analytical models have been developed with approximations on carrier density, material gain coefficients and spontaneous emissions [11]. In the following sections, theoretical models for SOAs are described, and a simplified numerical model is developed as well.

### 2.2.1 Introduction

We first begin with theoretical models for SOAs. Although an SOA is similar to a semiconductor laser, its mathematical models are different. Semiconductor lasers are generally analyzed using a set of rate equations governing photon and electron densities temporal variations in the laser cavity. Since high reflectivity mirrors are employed in the laser cavity, the photon and electron densities can be considered as constants throughout the laser cavity. However, this is not true for the modeling of SOA. In an SOA, the photon and electron densities strongly vary throughout the SOA cavity. These variations are strongly dependent on optical input power and a drive current. As a result, the photon and electron densities inside an SOA need to be modeled as both time and space dependent variables. Moreover, the photon density is described by a traveling wave equation [16].

There are several parameters are critical to the theoretical models of SOAs. The material gain coefficient model, waveguide internal loss, the electron carrier lifetime of spontaneous emissions and the fraction of total spontaneous emissions coupled into the signal and further amplified by an SOA.

The material gain coefficient determines the amplification capability of an optical amplifier. It depends on the density of electron carriers, amplification wavelengths. The waveguide internal loss includes two components: carrier independent loss and carrier-dependent absorption loss. The former is the intrinsic material loss, and latter results from intervalence band absorption. Both material gain and internal loss change the overall gain of an SOA. The carrier lifetime is determined by the recombination rate R, with $R = AN(z,t) + BN^2(z,t) + CN^3(z,t)$, the first two terms represent non-radiative recombination and spontaneous emission; the last term represents Auger

recombination. These coefficients are difficult to be determined to a high degree of accuracy. In general, this recombination rate is assumed to be linearly proportional to the carrier density, with $R=N/\tau$. The $\tau$ is the carrier lifetime of spontaneous emissions. This spontaneous carrier lifetime depends on optical power inside an SOA, and is affected by the stimulated emission [18].

In addition to an amplifier gain, the saturation power of an optical amplifier is an important parameter to evaluate performances of amplifiers. In the saturation state, the carrier density of electrons fails to provide enough electrons required by large input signal which causes carrier depletions. The saturation state of an amplifier is defined when a single pass gain of amplifier is a 3dB below the small signal gain. Large saturation power is preferred when an SOA is applied to linear amplification.

The confinement factor determines how much amplified power is restrained within the active region of the amplifier. An SOA with nonzero facets reflective can amplify backward signals and spontaneous emission. In general, this reflectivity of faces needs to be less than $10^{-5}$ [19]. Several analytical models have been reported, all these models use the gain model with polynomial approximations. Moreover, both carrier densities, internal loss are constants throughout an SOA cavity. These simplifications reduce these traveling wave equations for amplifiers to simple forms. As a result, analytical solutions for these simplified equations are obtainable. Without these simplifications and approximations, the system equations for an SOA have no analytical solution [11].

### 2.2.2 Numerical Model

Numerical modeling is particularly powerful for performance simulation and design optimization of SOAs with complex configurations or operating under stringent conditions [20]. There have been numerous broadband models established in the literature, among which the fully physics-based model [21] deals with the Maxwell-Bloch and carrier transport equations in a self-consistent manner [20]. However, it is computationally expensive, since the interactions among the optical field, the polarization, and the carrier are all treated microscopically [20].

In order to solve the SOA equation numerically, the SOA is divided into 30 sections as shown in Figure 2-4, we extracted a simplified 2D (longitudinal and vertical) model for an integrated SOA. With initial conditions, the carrier rate equation and traveling wave equations for signal and spontaneous emission are applied to each of these sections. This broadband time-domain model is established by combining the traveling wave with the wavelength slicing technique [14]. The spontaneous emission noise is modeled by a Gaussian distributed random source. Since the full-wave equations are used, the amplified spontaneous emission noise is coupled to the lasing mode and signal channels [20]. Therefore, our model considers the interaction among the carrier, the multichannel optical signal fields, and the spontaneous emission noise generated during the operations of such devices in a self-consistent manner [20].

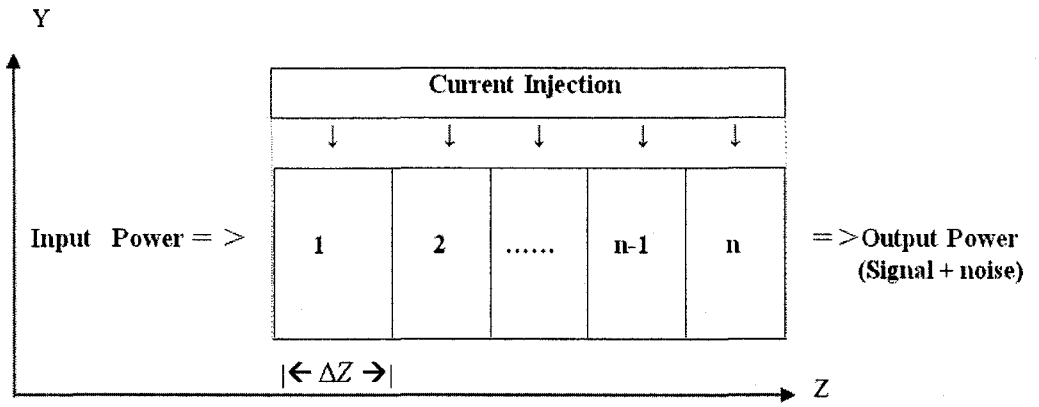


Figure 2-4: Schematic view of the device structure discretised in space insubsections of equal length.

Before we are going into detailed numerical modeling of SOA, the following assumptions have been made in order to simplify our discussion.

| | |
|---|---|
| A | Only forward optical wave propagates along the SOA |
| B | Wave with discrete frequencies has slow-varying envelop |
| C | Single transverse model is guided along the device. |
| D | Single operating frequency |
| E | P type layers on top & N type on the bottom |
| F | Waveguide structure is uniform along the propagate direction |
| G | Material takes no time to response the envelop varying of the optical wave |
| H | Wave is confined in $y$ direction, and only the spatial dependence along the optical wave propagation $z$ in the device is taken into consideration. |
| I | In the quantum well region, both non-radiative & spontaneous emission recombination takes place among both classical & non-classical carriers, where the stimulated emission recombination only take places among the non-classical carriers. |

Table 1: The assumptions for the numerical modeling of SOA.

In a semiconductor optical amplifier (SOA), both photon and electron densities vary temporally and spatially [11]. Since we assume power reflectivity at both facets (left and right) equal to zero, optical wave will only propagate in the forward direction.

As the forward optical wave propagates along SOA in the $+z$ direction, according to the slow-varying envelope approximation (SVEA), the following traveling-wave equation for the wavelength $\lambda_k$ is obtained: [13]

$$\begin{aligned}&\frac{1}{v_g}\frac{\partial}{\partial t}e^f(z,t,\lambda_k)+\frac{\partial}{\partial z}e^f(z,t,\lambda_k)\\&=[-j(\beta(\lambda_k)+\frac{1}{2}\Gamma\alpha_m g(z,t,\lambda_k))+\frac{1}{2}\Gamma g(z,t,\lambda_k)-\frac{1}{2}\alpha_s]e^f(z,t,\lambda_k)+\tilde{s}(z,t,\lambda_k)\end{aligned} \tag{1}$$

the last term $\tilde{s}(z,t,\lambda_k)$ is the noise during the wave propagation, and can be modeled as following: [13]

$$\tilde{s}(z,t,\lambda_k)\equiv -j\frac{e^{j(\omega_o t-\beta z)}}{n_{eff}\omega_o}\sqrt{\frac{\mu_0}{\varepsilon_o}}\int_{\Sigma}\frac{\partial}{\partial t}\bar{J}_{sp}\phi(x,y)dxdy \tag{2}$$

I did not use (2) for the calculation of the driving noise $\tilde{s}(z,t,\lambda_k)$ [V/m], since the term $\bar{J}_{sp}$ can't easily be evaluated. We can take a small step $d_z$ [m] along the wave propagation direction to integrate (1) at the steady state, we can get

$$e^f(z+d_z,t,\lambda_k)=e^{\Gamma[j\delta+jk_0\Delta n(N,P,T,W_0)-\frac{1}{2}\alpha]d_z}e^f(z,t,\lambda_k)+\tilde{s}(z,t,\lambda_k)d_z \tag{3}$$

multiplying (3) by its complex conjugate and factor $n_{eff}\sqrt{\varepsilon_0/\mu_0}/2$ [$1/\Omega$] on both side (3), we obtain:

$$p^f(z+d_z)=e^{\Gamma(g(N,P,W_0)-\alpha)d_z}P^f(z)+[n_{eff}d_z{}^2\sqrt{\varepsilon_0/\mu_0}\left|\tilde{s}(z,t,\lambda_k)\right|^2/2] \tag{4}$$

where the cross terms all disappear as the noise term has a random phase and their averaged contribution after the integration gives zero. The second term on the RHS

of (4) indicating the spontaneous noise power contribution in the local section $d_z$, and it's can be evaluated as: [13]

$$[n_{eff} d_z^2 \sqrt{\varepsilon_0 / \mu_0} \left|\tilde{s}(z,t,\lambda_k)\right|^2]/2 = \gamma \Gamma v_g g_{sp}(N,P,T,W_0)\hbar w_0 \tag{5}$$

the amplitude square of the noise contribution is:

$$\left|\tilde{s}(z,t,\lambda_k)\right|^2 = 2\sqrt{\mu_0 / \varepsilon_0}\ [\gamma \Gamma v_g g_{sp}(N,P,T,W_0)\hbar w_0 z / n_{eff} d_z^2] \tag{6}$$

and the autocorrelation of the noise function, which is modeled by a Gaussian random process, turns out to be: [13]

$$\begin{aligned} &\langle \left|\tilde{s}(z,t,\lambda_k)\right| \left|\tilde{s}(z',t',\lambda_k')\right| \rangle \\ &= 2\sqrt{\mu_0 / \varepsilon_0}\ [\gamma \Gamma v_g g_{sp}(N,P,T,W_0)\hbar w_0 z / n_{eff} d_z^2]\, \delta(t-t')\delta(z-z')\delta(\lambda_k - \lambda_k') \\ &= \left|\tilde{s}(z,t,\lambda_k)\right|^2 \delta(t-t')\delta(z-z')\delta(\lambda_k - \lambda_k') \end{aligned} \tag{7}$$

we can set : $2\sqrt{\mu_0 / \varepsilon_0}\ [\gamma \Gamma v_g g_{sp}(N,P,T,W_0)\hbar w_0 z / n_{eff} d_z^2] = P$ (power of the noise)

so $\tilde{s}(z,t) \cong \sqrt{p}\ e^{j\varphi}$ and $\varphi$ is the phase of noise modeled by a random process with uniform distribution over $[0, 2\pi]$. We can further simplify (7), and get it into the following form:

$$<\tilde{s}(z,t,\lambda_k)\ \tilde{s}^*(z',t',\lambda_k')> = \gamma \frac{R_{sp}(z,t,\lambda_k)}{d_z v_g} \delta(t-t')\delta(z-z')\delta(\lambda_k - \lambda_k') \tag{8}$$

Equation (8) can be evaluated by a Gaussian distributed or by a Poisson-distributed random number generator [22] satisfying the condition [23], [24]. The

function $\delta(\ )$ denotes the Dirac function. It would be more reasonable to take the occurrence of spontaneous events as a Poisson process, since such an assumption has a more sound and well-accepted theoretical foundation as discussed in [25]. On the theoretical basis, the law of large number and the central limit theorem state that the Poisson process can be approximated well by the uncorrelated Gaussian process [26].

The propagation constant for the wavelength $\lambda_k$ in the right hand side of (1) is:

$$\beta(\lambda_k) = \frac{2\pi n_{eff}}{\lambda_k} \tag{9}$$

Input signal field at the left facet of SOA is given as:

$$e^f(Z=0, t=0, \lambda_k) = \sqrt{\frac{\alpha_{in} P_{in}(t)}{h\nu_k w d v_g}} \tag{10}$$

The output power of the $k_{th}$ channel from the right facet of SOA can be expressed as:

$$P_{out} = h\nu_k A_{eff} v_g \alpha_{out} \left| e^f(L, t, , \lambda_k) \right|^2 \tag{11}$$

Affected by the random noise generator, the complex field calculated through the above governing equations must fluctuate in time; therefore, the output power can only be obtained by taking average over a time period after the stead state is reached [13].

The center wavelength at the $k_{th}$ channel is:

$$\lambda_k = \lambda_{\min} + k\Delta\lambda \tag{12}$$

Where $\lambda_{\max} = \lambda_{\min} + N_d \Delta\lambda \qquad k = 1,2,3,\ldots,N_d$

All the optical wave and power equations at different wavelength segments are coupled through the "carrier-sharing" mechanism, governed by the following carrier rate equation:

$$\frac{\partial N(z,t)}{\partial t} = \eta \frac{I}{qdwL} - [A + BN(z,t) + CN^2(z,t)]N(z,t) - R_{stim}(z,t) \tag{13}$$

The stimulated emission rate of the propagation wave is given by:

$$R_{stim}(z,t) = \sum_{k=1}^{N_d} \Gamma v_g g(z,t,\lambda_k) \left| e^f(z,t,\lambda_k) \right|^2 \tag{14}$$

In (14), the direct interference between the fields of different wavelengths is ignored. Consequently, nonlinear phenomena such as the wave mixing and the mode locking cannot be treated by this model [13].

The spontaneous emission rate of the propagation wave is given by:

$$R_{sp}(z,t) = n_{sp} R_{stim}(z,t) \tag{15}$$

The material gain of SOA at the $k$ th channel is calculated based on the following polynomial approximation:

$$g(z,t,\lambda_k) \cong \alpha(N(z,t) - N_{tr})[1 - (\frac{\lambda_k - \lambda_p}{\lambda_w})^2] \tag{16}$$

The model parameters used for the simulation are summarized in the Table.2, which are typical for such a device with the material system chosen. Wavelength

dependence of the spontaneous coupling coefficient is ignored for the sake of simplicity [13].

| Variable | Physical meaning | Type | Dimension | Value |
|---|---|---|---|---|
| $e^f(z,t,\lambda_k)$ | Slow-varying envelop at the $K_{th}$ channel | Unknown variable | $1/cm^{3/2}$ | |
| $N(z,t)$ | Carrier density | Unknown variable | $1/cm^3$ | |
| $g(z,t,\lambda_k)$ | Material gain | Intermediate variable | $1/cm$ | |
| $R_{sp}(z,t,\lambda_k)$ | Spontaneous emission rate | Intermediate variable | $1/s\text{-}cm^3$ | |
| $R_{stim}(z,t)$ | Stimulated emission rate | Intermediate variable | $1/s\text{-}cm^3$ | |
| $\tilde{s}(z,t,\lambda_k)$ | Locally generated spontaneous emission noise source | Intermediate variable | $1/cm^{5/2}$ | |
| $v_k$ | Frequency corresponding to wavelength $\lambda_k$ : $v_k = c/\lambda_k$ | Intermediate variable | $Hz$ | |
| $P_{in}(t)$ | Input power at the $k_{th}$ wavelength channel | Input variable | $W$ | $1\times10^{-6}$ |
| $v_g$ | Group velocity: $v_g = c/n_g$ | Constant | $cm/s$ | $0.8\times10^{10}\,cm/s$ |
| $A_{eff}$ | Effective active area: $A_{eff} = wd/\Gamma$ | Constant | $cm^2$ | $1\times10^{-8}$ |
| $N_d$ | Number of subsections introduced by spectrum slicing | Constant | dimensionless | 50 |
| $N_{tr}$ | Transparent carrier density | Constant | $1/cm^3$ | $1\times10^{18}$ |
| $n_{sp}$ | Population-inversion factor | Constant | dimensionless | 1.7 |
| $\Gamma$ | Confinement factor | Constant | dimensionless | 0.3 |
| $\alpha_m$ | Linewidth enhancement factor | Constant | dimensionless | -4 |
| $\alpha_s$ | Modal loss | Constant | $1/cm$ | 20 |

| | | | | |
|---|---|---|---|---|
| $\gamma$ | Spontaneous emission coupling coefficient | Constant | dimensionless | 0.0001 |
| $R_l$ | Power reflectivity at the left (input) facet | Constant | dimensionless | 0 |
| $R_r$ | Power reflectivity at the right (output) facet | Constant | dimensionless | 0 |
| $\alpha_{in}$ | Input coupling loss from the fiber to the device waveguide | Constant | dimensionless | 0.5 |
| $\alpha_{out}$ | Output coupling loss from the device waveguide to the fiber | Constant | dimensionless | 0.5 |
| $w$ | Active layer width | Constant | $cm$ | $1.5\times10^{-4}$ |
| $d$ | Active layer thickness | Constant | $cm$ | $0.2\times10^{-4}$ |
| $L$ | Device length | Constant | $cm$ | 0.06 |
| $\eta$ | Current injection efficient | Constant | dimensionless | 1 |
| $n_{eff}$ | Effective refractive index | Constant | dimensionless | 3.2 |
| $n_g$ | Group refractive index | Constant | dimensionless | 3.7 |
| q | Unit electron charge | Constant | $c$ | $1.6\times10^{-19}$ |
| $c$ | Speed of light | Constant | $cm/s$ | $3\times10^{10}$ |
| $A$ | SRH recombination coefficient | Constant | $1/s$ | $2.8\times10^{8}$ |
| $B$ | Spontaneous emission and bimolecular recombination coefficient | Constant | $cm^3/s$ | $1\times10^{-10}$ |
| $C$ | Auger recombination coefficient | Constant | $cm^6/s$ | $3.5\times10^{-29}$ |
| $h$ | Plank's constant | Constant | $J-s$ | $6.6\times10^{-34}$ |
| $\lambda_p$ | Peak gain wavelength | Constant | $cm$ | $1.55\times10^{-4}$ |
| $\lambda_w$ | Parabolic-shaped gain profile width | Constant | $cm$ | $5\times10^{-6}$ |
| $\alpha$ | Differential gain | Constant | $cm^2$ | $4\times10^{-16}$ |
| $\Delta z$ | The width for spatial discretization | Constant | $cm$ | $2\times10^{-3}$ |
| $n$ | Number of subsections | Constant | | 30 |
| $\Delta t$ | The time domain marching step | Constant | $s$ | $2.5\times10^{-13}$ |
| $I$ | The Bias injection current of SOA | Constant | $A$ | $1\times10^{-3}$ |

Table 2: Summary of SOA parameters.

In the following section, a numerical solver based on the finite difference method (FDM) is first developed. The numerical solution to a traveling wave amplifier i.e., with $R_l = R_r = 0$ is considered.

## 2.3 Implementation

Based on the numerical model described in 2.2.2, we proposed a numerical solver in order to implement these governing equations extracted from a 2D (longitudinal and vertical) model for an integrated SOA.

Step. 1

At initial input condition (Assume $z = 0 \quad t = 0$):

$$R_{stim} = 0 \qquad \frac{\partial N(z,t)}{\partial t} = 0$$

solve the cubic equation (13) respect to $N(z,t)$, we can get the initial value for $N(z=0, t=0)$, given $I$ is the bias current of SOA.

After substitute initial condition into (13), it is simplified to the following form:

$$0 = \eta \frac{I}{qdwL} - [A + B \bullet N(0,0) + C \bullet N^2(0,0)]N(0,0) \tag{17}$$

Since all the other parameters are known, we can solve for $N(z=0, t=0)$.

Step. 2

After substitute the initial value:

$N(z=0,t=0)$

into gain's equation (16), we can get

the initial value for the gain:

$g(z=0,t=0,\lambda_k)$.

After we substitute $N(0,0)$ into (16), it is simplified to the following form

$$g(0,0,\lambda_k) \cong \alpha(N(0,0)-N_{tr})[1-(\frac{\lambda_k-\lambda_p}{\lambda_w})^2] \qquad (18)$$

Since all the other parameters are known, we can solve for $g(z=0,t=0,\lambda_k)$

Step.3

By using the input condition from equation (10)

$e^f(z=0,t=0,\lambda_k)$

and gain's initial value $g(z=0,t=0,\lambda_k)$ from

Step. 2, we can get initial value of $R_{stim}$ from

equation (14).

The input wave is derived from $e^f(0,0,\lambda_k) = \sqrt{\frac{\alpha_{in} P_{in}}{h\nu_k w d v_g}}$, and $g(0,0,\lambda_k)$ is already know from Step. 2. We can substitute them into (14), and get the following equation:

$$R_{stim}(0,0) = \sum_{k=1}^{N_d} \Gamma v_g g(0,0,\lambda_k) \left| e^f(0,0,\lambda_k) \right|^2 \tag{19}$$

Since all the parameters are know, $R_{stim}(z=0,t=0)$ can be solved.

Step 4

| |
|---|
| Substitute initial value of $R_{stim}(z=0,t=0)$ into equation (15), we get initial value of $R_{sp}(z=0,t=0)$ |

After we substitute $R_{stim}(0,0)$ into equation (15) , we can get

$$R_{sp}(0,0) = n_{sp} R_{stim}(0,0) \tag{20}$$

Since all the other parameters are known, the $R_{sp}(z=0,t=0)$ can be solved.

Step.5

Substitute initial value of $R_{sp}(z=0,t=0,\lambda_k)$ into equation (8). By using the Gaussian distributed random number generator, we can get initial value of $\tilde{s}(z=0,t=0,\lambda_k)$

**Note**: the $\tilde{s}(z=0,t=0,\lambda_k)$ at this stage is still zero, since the input light is still at the right surface of the cavity, and have not enter the device yet

After we substitute $R_{sp}(0,0,\lambda_k)$ into equation (8), we can get the following equation:

$$<\tilde{s}(0,0,\lambda_k)\,\tilde{s}^*(0',0',\lambda_k')>=\gamma\frac{R_{sp}(0,0,\lambda_k)}{d_z v_g}\delta(t-t')\delta(z-z')\delta(\lambda_k-\lambda_k') \qquad (21)$$

This equation represents the noise during the wave propagation, and can be modeled by a Gaussian distributed random number generator with average equals to zero, and variance equals to $\sqrt{\gamma\frac{R_{sp}(z,t,\lambda_k)}{d_z v_g}}$. Even though we can get a non-zero output for $\tilde{s}(z=0,t=0,\lambda_k)$ at this stage, this number suppose to be zero in theory, because the light at $(z=0,t=0)$ has not enter the SOA yet. In other words, there should not be any generated noise at this point, i.e. $\tilde{s}(z=0,t=0,\lambda_k)$=0.

Step. 6

| |
|---|
| Substitute initial values of $\tilde{s}(z=0,t=0,\lambda_k)$, which is zero at this stage, and $g(z=0,t=0,\lambda_k)$ into equation (1). By using the $e^f(z=0,t=0,\lambda_k)$ from equation (10) as initial condition, we can update the optical wave from $e^f(z=0,t=0,\lambda_k)$ to $e^f(z=\Delta z,t=\Delta t,\lambda_k)$ by using following form of finite difference approximation |

Since the solutions for $\tilde{s}(0,0,\lambda_k)$, $g(0,0,\lambda_k)$, and $e^f(0,0,\lambda_k)$ are known, we can substitute them into equation (1) and solve it through following procedures:

$$(\frac{1}{v_g}\frac{\partial}{\partial t}+\frac{\partial}{\partial z})e^f(z,t,\lambda_k)$$
$$=[-j(\beta(\lambda_k)+\frac{1}{2}\Gamma\alpha_m g(z,t,\lambda_k))+\frac{1}{2}\Gamma g(z,t,\lambda_k)-\frac{1}{2}\alpha_s]e^f(z,t,\lambda_k)+\tilde{s}(z,t,\lambda_k)$$

According to the finite difference method, equation (1) can be rearranged as the following:

$$\frac{1}{v_g}\frac{\partial}{\partial t}e^f(z,t,\lambda_k)=\frac{e^f(z,t+\Delta t,\lambda_k)-e^f(z,t,\lambda_k)}{v_g\Delta t}$$

$$\frac{\partial}{\partial z}e^f(z,t,\lambda_k)=\frac{e^f(z,t,\lambda_k)-e^f(z-\Delta z,t,\lambda_k)}{\Delta z}$$

$$\mathrm{A}=[-j(\beta(\lambda_k)+\frac{1}{2}\Gamma\alpha_m g(z,t,\lambda_k))+\frac{1}{2}\Gamma g(z,t,\lambda_k)-\frac{1}{2}\alpha_s]$$

Which are equivalent to the following equation format:

$$\frac{e^f(z,t+\Delta t,\lambda_k)-e^f(z,t,\lambda_k)}{v_g\Delta t}+\frac{e^f(z,t,\lambda_k)-e^f(z-\Delta z,t,\lambda_k)}{\Delta z}$$
$$=\mathrm{A}\,e^f(z,t,\lambda_k)+\tilde{s}(z,t,\lambda_k) \qquad (22)$$

According to Figure.2-4, we have vertically divided SOA into $n$ segments, and the width for each segment is $\Delta z$. The time taking the wave propagates through each segment is $\Delta t$. The total displacement for the wave to propagate is $z$, and the corresponding time is $t$. Based on the relations between time and displacement, the following equations could be applied

$$\begin{aligned} z &= n\Delta z \\ t &= k\Delta t \\ n &=0,1,2,\ldots,30. \\ k &=0,1,2,\ldots,30. \end{aligned} \qquad (23)$$

Since $z$ and $t$ change spontaneously, we can replace them with $n$ and $k$ respectively. I.e. $e^f(z,t,\lambda_k)$ is the same as $e^f(n\Delta z,k\Delta t,\lambda_k)$ and $e^f(n,k,\lambda_k)$.

$$\frac{e^f(n,k+1,\lambda_k)-e^f(n,k,\lambda_k)}{v_g\Delta t}+\frac{e^f(n,k,\lambda_k)-e^f(n-1,k,\lambda_k)}{\Delta z} =\mathrm{A}\,e^f(n,k,\lambda_k)+\tilde{s}(n,k,\lambda_k) \tag{24}$$

$$\frac{v_g\Delta t}{\Delta Z}=m \tag{25}$$

Note that $m$ is a constant number and $m \in [0,1]$

We can transform the above equation again to the following format:

$$\frac{e^f(n+1,k+1,\lambda_k)-e^f(n+1,k,\lambda_k)}{v_g\Delta t}+\frac{e^f(n+1,k,\lambda_k)-e^f(n,k,\lambda_k)}{\Delta z} =\mathrm{A}\,e^f(n,k,\lambda_k)+\tilde{s}(n,k,\lambda_k) \tag{26}$$

$$\frac{1}{m\Delta z}[e^f(n+1,k+1,\lambda_k)-e^f(n+1,k,\lambda_k)+m\,e^f(n+1,k,\lambda_k)-me^f(n,k,\lambda_k)]$$

$$=\mathrm{A}\,e^f(n,k,\lambda_k)+\tilde{s}(n,k,\lambda_k) \tag{27}$$

$$e^f(n+1,k+1,\lambda_k)-e^f(n+1,k,\lambda_k)$$

$$=m\Delta z\ [\mathrm{A}\,e^f(n,k,\lambda_k)+\tilde{s}(n,k,\lambda_k)]-me^f(n+1,k,\lambda_k)+me^f(n,k,\lambda_k) \tag{28}$$

$$
\begin{aligned}
& e^f(n+1,k+1,\lambda_k) \\
& = m\Delta z\ [\mathrm{A}\, e^f(n,k,\lambda_k) + \tilde{s}(n,k,\lambda_k)] + (1-m)e^f(n+1,k,\lambda_k) + me^f(n,k,\lambda_k) \\
& = (1-m)e^f(n+1,k,\lambda_k) + m\,(1+\mathrm{A}\,\Delta z)\, e^f(n,k,\lambda_k) + m\Delta z\ \tilde{s}(n,k,\lambda_k)
\end{aligned} \tag{29}
$$

Since $n$ and $k$ share the same common values and change spontaneously, we can use $k$ 's value to replace $n$, and modify the above equation to the following format:

$$
\begin{aligned}
& e^f(n=k+1,k+1,\lambda_k) \\
& = (1-m)e^f(n=k+1,k,\lambda_k) \\
& + m\,(1+[-j(\beta(\lambda_k) + \frac{1}{2}\Gamma\alpha_m g(z,t,\lambda_k)) + \frac{1}{2}\Gamma g(z,t,\lambda_k) - \frac{1}{2}\alpha_s]\ \Delta z)\, e^f(n=k,k,\lambda_k) \\
& + m\Delta z\ \tilde{s}(n=k,k,\lambda_k)
\end{aligned} \tag{30}
$$

when $k$ equals to zero, the above equation becomes:

$$
\begin{aligned}
& e^f(n+1,1,\lambda_k) \\
& = (1-m)e^f(n+1,0,\lambda_k) + m\,(1+\mathrm{A}\,\Delta z)\, e^f(n,0,\lambda_k) + m\Delta z\ \tilde{s}(n,0,\lambda_k)
\end{aligned} \tag{31}
$$

Note that $e^f(n,0,\lambda_k)=0$ for $n \neq 0$, because there is no input at nth segment at time equals to zero or initial time. As the value for $n$ increases from 0 to 29, the above equation becomes:

$$
\begin{aligned}
&e^f(1,1,\lambda_k)\\
&=(1-m)e^f(1,0,\lambda_k)+\ m\,(1+\mathrm{A}\,\Delta z)\,e^f(0,0,\lambda_k)+m\Delta z\ \tilde{s}(0,0,\lambda_k)\\
&=m\,(1+\mathrm{A}\,\Delta z)\,e^f(0,0,\lambda_k)
\end{aligned}
\tag{32}
$$

$$
\begin{aligned}
&e^f(2,1,\lambda_k)\\
&=(1-m)e^f(2,0,\lambda_k)+\ m\,(1+\mathrm{A}\,\Delta z)\,e^f(1,0,\lambda_k)+m\Delta z\ \tilde{s}(1,0,\lambda_k)\\
&=m\Delta z\ \tilde{s}(1,0,\lambda_k)
\end{aligned}
\tag{33}
$$

.....

$$
\begin{aligned}
&e^f(30,1,\lambda_k)\\
&=(1-m)e^f(30,0,\lambda_k)+\ m\,(1+\mathrm{A}\,\Delta z)\,e^f(29,0,\lambda_k)+m\Delta z\ \tilde{s}(29,0,\lambda_k)\\
&=m\Delta z\ \tilde{s}(29,0,\lambda_k)
\end{aligned}
\tag{34}
$$

From the above equations, $e^f(n+1,1,\lambda_k)$ $n$ =0,1,2,...,29. are known paremeters.

when $k$=1, repeat the above procedures again, and we can get the following equations:

$$
\begin{aligned}
&e^f(1,2,\lambda_k)\\
&=(1-m)e^f(1,1,\lambda_k)+\ m\,(1+\mathrm{A}\,\Delta z)\,e^f(0,1,\lambda_k)+m\Delta z\ \tilde{s}(0,1,\lambda_k)
\end{aligned}
$$

$$
\begin{aligned}
&e^f(2,2,\lambda_k)\\
&=(1-m)e^f(2,1,\lambda_k)+\ m\,(1+\mathrm{A}\,\Delta z)\,e^f(1,1,\lambda_k)+m\Delta z\ \tilde{s}(1,1,\lambda_k)
\end{aligned}
$$

.....

$$
\begin{aligned}
&e^f(30,2,\lambda_k)\\
&=(1-m)e^f(30,1,\lambda_k)+\ m\,(1+\mathrm{A}\,\Delta z)\,e^f(29,1,\lambda_k)+m\Delta z\ \tilde{s}(29,1,\lambda_k)
\end{aligned}
\tag{35}
$$

Note: 1. $e^f(0,0,\lambda_k)=e^f(0,1,\lambda_k)....=\ e^f(0,30,\lambda_k)=\sqrt{\dfrac{\alpha_{in}P_{in}}{h\nu_k w d v_g}}$

2. The values for $e^f(n+1,n,\lambda_k)$ $n$=0,1,2,...,29 had already known from previous repetitions.

3. $e^f(1,1,\lambda_k)$ is the same as $e^f(\Delta z,\Delta t,\lambda_k)$

We have to repeat above procedure, i.e. $k$=2,3,....29 until get the value for $e^f(30\Delta z,30\Delta t,\lambda_k)$, which will be the output wave envelop of SOA

Step. 7

| |
|---|
| Substitute the updated value $e^f(z=\Delta z,t=\Delta t,\lambda_k)$ into equation (14), we can get the updated value $R_{stim}(z=\Delta z,t=\Delta t)$ Note: we still use previous calculated gain's value $g(z=0,t=0,\lambda_k)$ during this calculation. |

After we had the value for $e^f(\Delta z,\Delta t,\lambda_k)$ from Step.6, substitute it into equation (14) We can get the following equation:

$$R_{stim}(\Delta z,\Delta t)=\sum_{k=1}^{N_d}\Gamma v_g g(0,0,\lambda_k)\left|e^f(\Delta z,\Delta t,\lambda_k)\right|^2 \tag{36}$$

the updated value for $R_{stim}(\Delta z,\Delta t)$ can be solved. Note that at this step, we used $g(0,0,\lambda_k)$ for the calculation. This is a close approximation, because we only can update gain's value after this step.

Step.8

Repeat Step.1. But the value of $R_{stim}$ has been updated from Step 7. Since the light has reached the 2nd segment by this time, LHS of equation (13) $\frac{\partial N(z,t)}{\partial t}$ does not equal to zero anymore. The equation (13) can be solved by the following form of finite difference approximation.

Since the light has already reached the 2nd segment, the value for $\frac{\partial N(z,t)}{\partial t}$ no long equals to zero. The equation (13) becomes the following format:

$$\frac{\partial N(z,t)}{\partial t} = \eta \frac{I}{qdwL} - [A + BN(0,0) + CN^2(0,0)]N(0,0) - R_{stim}(\Delta z, \Delta t) \qquad (37)$$

Note that the value for $R_{stim}(\Delta z, \Delta t)$ has already obtained from Step.6. We can apply finite difference method to this equation, and get to the following format:

$$\frac{N(\Delta z, \Delta t, \lambda_k) - N(0,0,\lambda_k)}{\Delta t} = \eta \frac{I}{qdwL} - [A + BN(0,0,\lambda_k) + CN^2(0,0,\lambda_k)]N(0,0,\lambda_k) - R_{stim}(\Delta z, \Delta t) \qquad (38)$$

Note that $N(\Delta z, \Delta t, \lambda_k)$ is the carrier density in the 2nd segment of SOA.

$$N(\Delta z, \Delta t, \lambda_k)$$
$$= \Delta t[\eta \frac{I}{qdwL} - [A + BN(0,0,\lambda_k) + CN^2(0,0,\lambda_k)]N(0,0,\lambda_k) - R_{stim}(\Delta z, \Delta t)] + N(0,0,\lambda_k) \quad (39)$$

Since all the other parameters in this equation are known, we can solve for updated value of carrier density $N(\Delta z, \Delta t, \lambda_k)$ through finite difference method

Step.9

> Repeat Step.2. Substitute the updated value
>
> $$N(z = \Delta z, t = \Delta t, \lambda_k)$$
>
> from equation (13) into equation (16), we can get the updated gain value:
>
> $$g(z = \Delta z, t = \Delta t, \lambda_k)$$
>
> for the 2nd segment.

After substitute $N(\Delta z, \Delta t, \lambda_k)$ into equation (16), we can get the following equation:

$$g(\Delta z, \Delta t, \lambda_k) \cong \alpha(N(\Delta z, \Delta t, \lambda_k) - N_{tr})[1 - (\frac{\lambda_k - \lambda_p}{\lambda_w})^2] \quad (40)$$

The updated value $g(z = \Delta z, t = \Delta t, \lambda_k)$ for the 2nd segment can be obtained based on the above equation.

Step.10

Repeat Step.4. Substitute updated value

$$R_{stim}(z=\Delta z, t=\Delta t, \lambda_k)$$

into equation (14), we get updated value

$$R_{sp}(z=\Delta z, t=\Delta t, \lambda_k).$$

After $R_{stim}(\Delta z, \Delta t, \lambda_k)$ is obtained in Step.9, the updated value $R_{stim}(z=\Delta z, t=\Delta t, \lambda_k)$ can be obtained as well.

$$R_{sp}(\Delta z, \Delta t, \lambda_k) = n_{sp} R_{stim}(\Delta z, \Delta t, \lambda_k) \tag{41}$$

Step. 11

Repeat Step.5 Substitute updated value $R_{sp}(z=\Delta z, t=\Delta t, \lambda_k)$ into equation (8). By using the Gaussian distributed random number Generator, we can get updated value $\tilde{s}(z=\Delta z, t=\Delta t, \lambda_k)$.

**Note:** the value $\tilde{s}(z=\Delta z, t=\Delta t, \lambda_k)$, from this stage on, will no longer equal to zero anymore since the light has enter the cavity

After we get the updated value for $R_{sp}(\Delta z, \Delta t, \lambda_k)$, we put it into equation (8)

$$<\tilde{s}(\Delta z, \Delta t, \lambda_k)\ \tilde{s}^*(\Delta z', \Delta t', \lambda_{k'})>=\gamma \frac{R_{sp}(\Delta z, \Delta t, \lambda_k)}{d_z v_g}\delta(t-t')\delta(z-z')\delta(\lambda_k-\lambda_{k'}) \qquad (42)$$

this equation represents the noise during the wave propagation, and can be modeled by a Gaussian distributed random number generator with average equals to zero, and variance equals to $\sqrt{\gamma \frac{R_{sp}(z,t,\lambda_k)}{d_z v_g}}$. We used a Gaussian distributed random number generator to model this equation, and the updated value $\tilde{s}(\Delta z, \Delta t, \lambda_k)$ can be obtained. Since the wave has already entered the SOA, the value for $\tilde{s}(\Delta z, \Delta t, \lambda_k)$ should be no longer equals to zero anymore.

Step. 12

| |
|---|
| Repeat Step.6. Substitute updated values of $\tilde{s}(z=\Delta z, t=\Delta t, \lambda_k)$ and $g(z=\Delta z, t=\Delta t, \lambda_k)$ into equation (1). By using updated value $e^f(z=\Delta z, t=\Delta t, \lambda_k)$ from Step.6 as initial condition, we can update the optical wave from the 1st segment $e^f(z=\Delta z, t=\Delta t, \lambda_k)$ to the 2nd segment $e^f(z=2\Delta z, t=2\Delta t, \lambda_k)$ by the these procedures described after Step.6. |

The updated values for $\tilde{s}(\Delta z, \Delta t, \lambda_k)$ and $g(\Delta z, \Delta t, \lambda_k)$ can be put back into equation (1). Since we already had the value of $e^f(\Delta z, \Delta t, \lambda_k)$, it can be used as an initial condition to solve this equation.

$$e^f(2,2,\lambda_k) = (1-m)e^f(2,1,\lambda_k) + m(1+\mathrm{A}\Delta z)e^f(1,1,\lambda_k) + m\Delta z\ \tilde{s}(1,1,\lambda_k) \quad (43)$$

All the parameters in this equation have already been calculated from previous steps, the value for $e^f(2\Delta z, 2\Delta t, \lambda_k)$ can be obtained easily.

Step. 13

Repeat from Step 7 to Step 12. When the optic wave reaches Output end, we get $e^f(z=L, t=\frac{L}{v_g}, \lambda_k)$, which equivalent to $e^f(z=30\Delta z, t=30\Delta t, \lambda_k)$.

Substitute $e^f(z=30\Delta z, t=30\Delta t, \lambda_k)$ into equation (11), the output power will be eventually calculated.

*the end of numerical solver*

After the wave propagates through the SOA, we can get the output envelope value $e^f(30\Delta z, 30\Delta t, \lambda_k)$ by repeating from Step.7 to Step.12. Substitute this value into equation (11)

$$P_{out} = h\nu_k A_{eff} v_g \alpha_{out} \left| e^f (30\Delta z, 30\Delta t, \lambda_k) \right|^2 \quad (44)$$

The final output power from SOA will be obtained.

## 2.4 Simulation of Gain Dependence on Device Parameters

As the cavity length equals to 0.08cm, the gain vs input power curve is generated as following (vertical axis for gain in dB unit, horizontal axis for input power in dBm Unit):

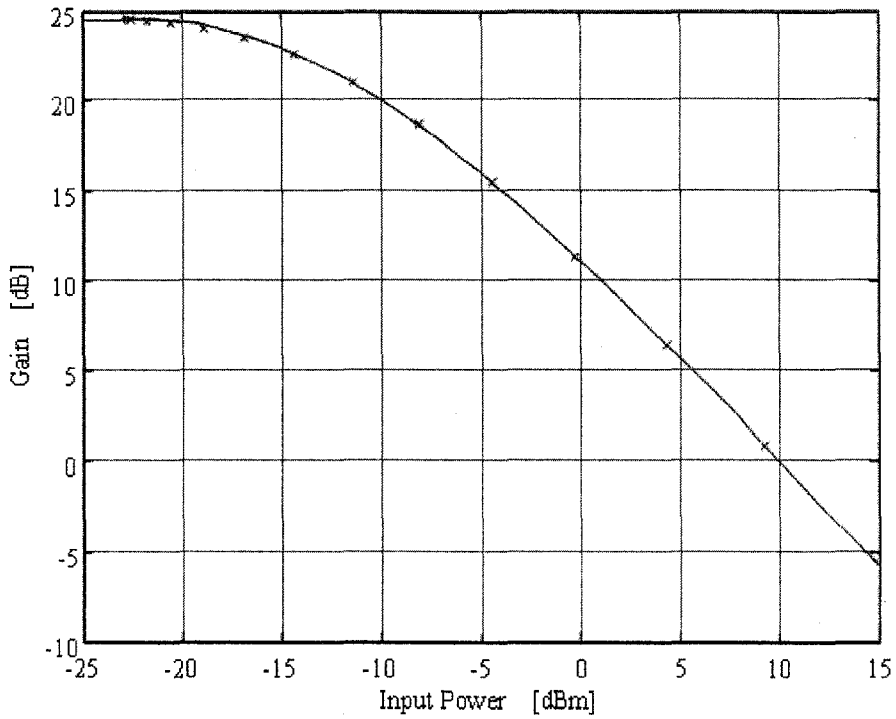


Figure 2-5: The graph for gain vs. input power, when the cavity length equals to 0.08cm.

In order to show the effectiveness of SOA's gain property, we simulated two cases for the SOA. In the first case, we used randomly generated return-to-zero

rectangular waveform. The incident power is 3.163 mW, which approximately correspond to 5 dBm in the horizontal axis of Figure 2-5. The data rate is 1 Gbit/s, and the total time duration for the waveform is 127 ns. This is shown in Figure 2-6. After the amplification of SOA, the output waveform is shown is Figure 2-7, and it approximately equals to 11 mW.

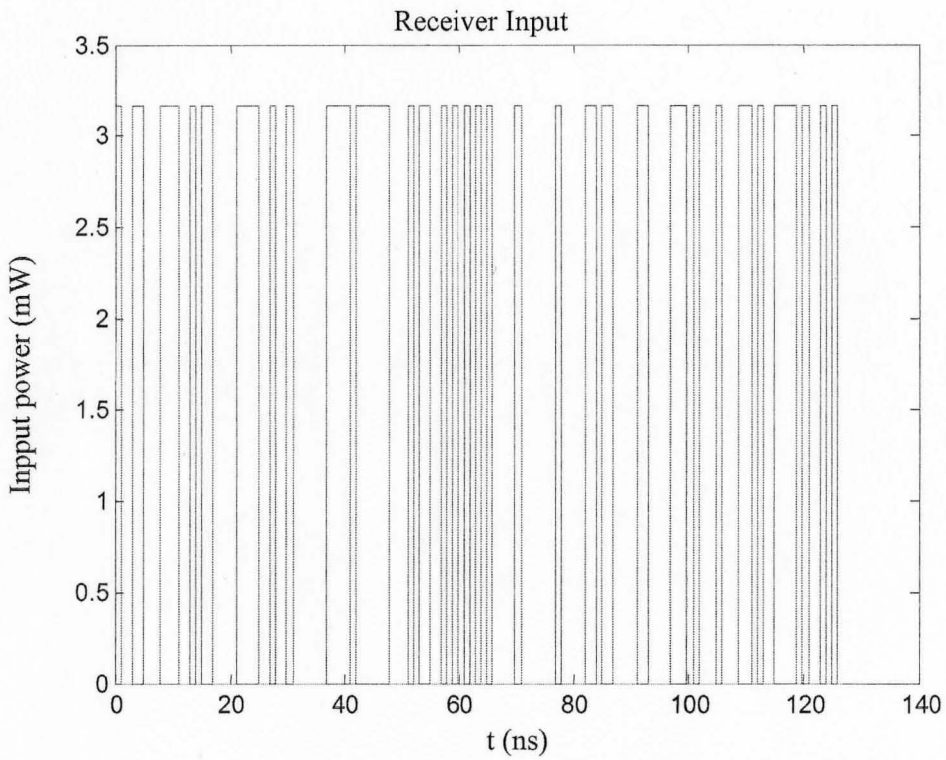


Figure 2-6: The schematic view of return-to-zero input waveform at incident power equals to 3.163 mW.

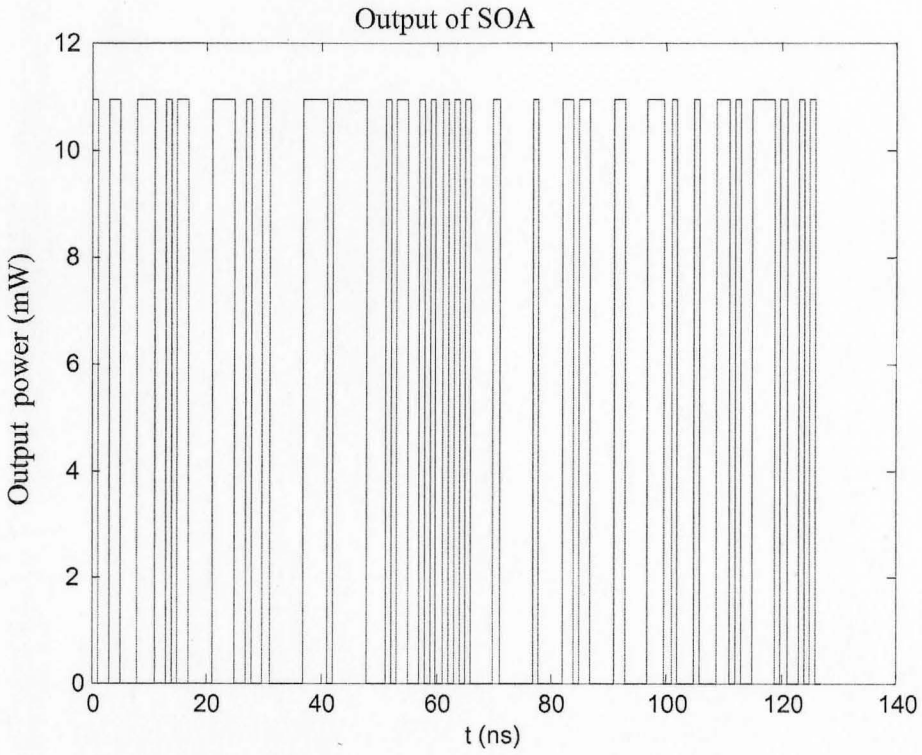


Figure 2-7: The schematic view of return-to-zero output waveform at incident power equals to 3.163 mW.

In the second case, we also used randomly generated return-to-zero rectangular waveform. The incident power is 0.3163 mW, which approximately correspond to -5 dBm in the horizontal axis of Figure 2-5. The data rate is 1 Gbit/s, and the total time duration for the waveform is 127 ns. This is shown in Figure 2-8. After the amplification of SOA, the output waveform is shown is Figure 2-9, and it approximately equals to 13 mW.

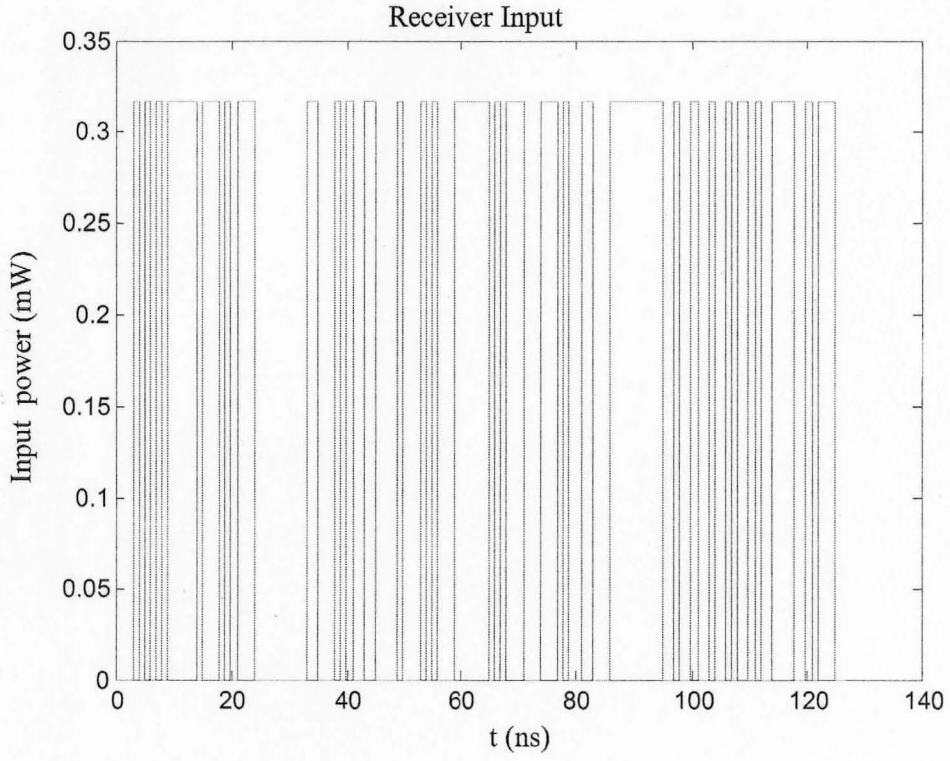


Figure 2-8: The schematic view of return-to-zero input waveform at incident power equals to 0.3163 mW.

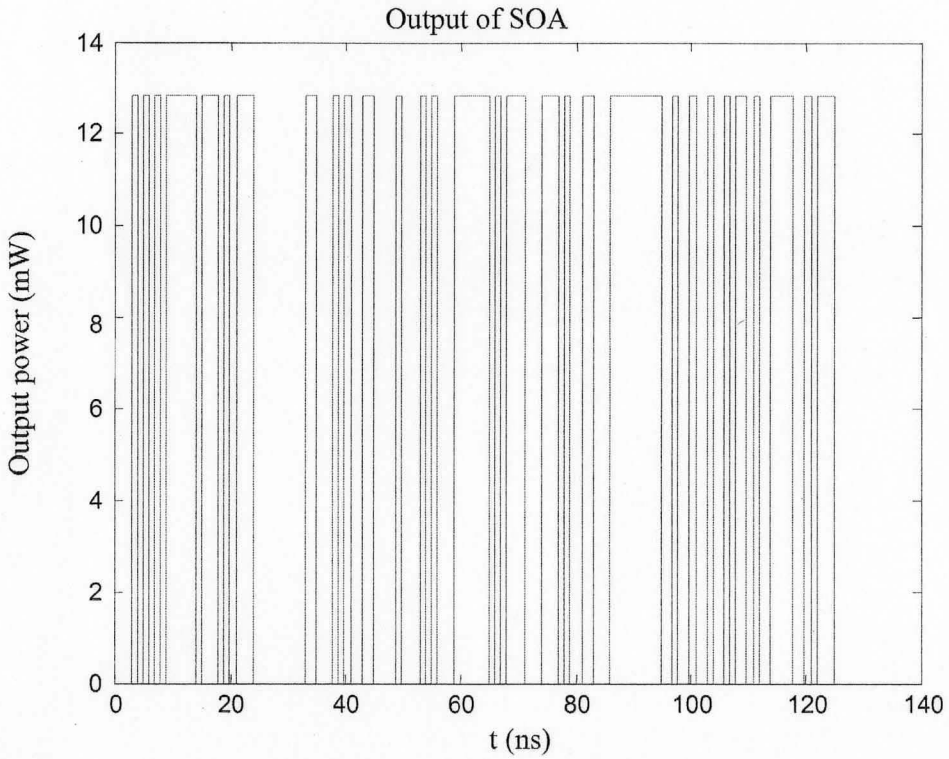


Figure 2-9: The schematic view of return-to-zero output waveform at incident power equals to 0.3163 mW.

### 2.4.1 Gain Dependence on Cavity Length

The special gain properties of SOA have always been the main focus, and it can be adjusted by changing several parameters. One interesting effect is the relationship between SOA's gain and its cavity length $L$. Theoretically, as the cavity length reduces/increases, the forward propagate wave (photons) gets amplified through a shorter/longer distance, although the gain per unit length increases/decreases, the total gain still decreases/increases, However, this is may not be the case in reality. During the simulation, we noticed that as the cavity length reduces/increases, the total gain

increases/reduces which is contrary to the theoretical results. Through our careful analysis, the detailed explanation and graphical illustrations are given below.

Based on our careful study and comparison with other papers, the SOA's gain and its cavity length should approximately satisfy the following relation:

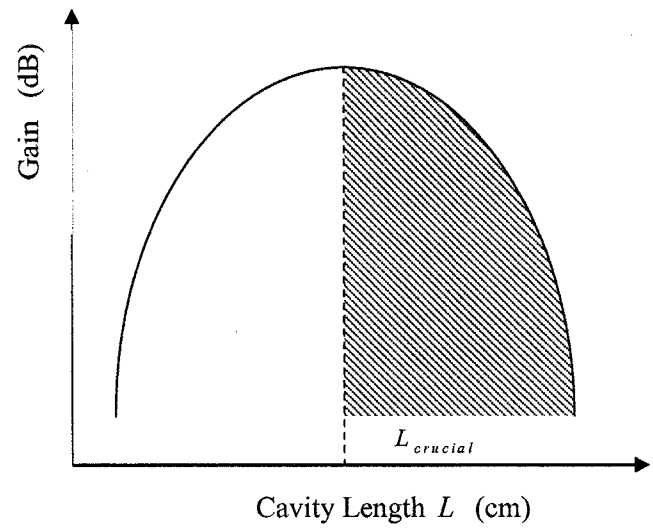


Figure 2-10: The graphical relation between SOA's gain and its cavity length.

As shown in the Figure 2-10, there are two regions separated by the crucial cavity length $L_{crucial}$. On the left side of $L_{crucial}$, the SOA's gain is positively proportional to its cavity length. However, on the right side of $L_{crucial}$, the SOA's gain is reversibly proportional to its cavity length. Due to the parameters of SOA we have used during simulation, our results consist with the graph located at right side of $L_{crucial}$ (shaded region).

As shown in the Figure 2-11, when the cavity length reduces from 0.08cm to 0.07cm, the curves in Figure 2-11 shift up dramatically, and the initial gain (G) increases from 24 dB to 40 dB approximately.

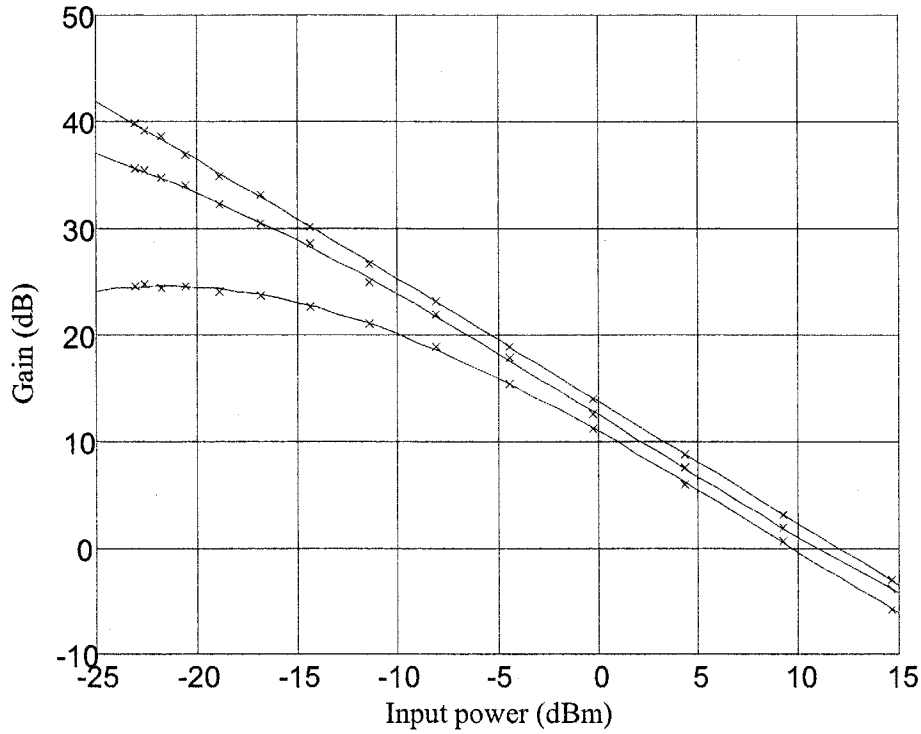


Figure 2-11: The graphs for gain vs. input power, from the bottom curve to the top, the cavity length equals to 0.08cm, 0.075cm, and 0.07cm respectively.

As shown in the Figure 2-12, when the cavity length increases from 0.08cm to 0.085cm, the curves shift down dramatically, and the initial gain decreases from 24 dB to 10 dB approximately.

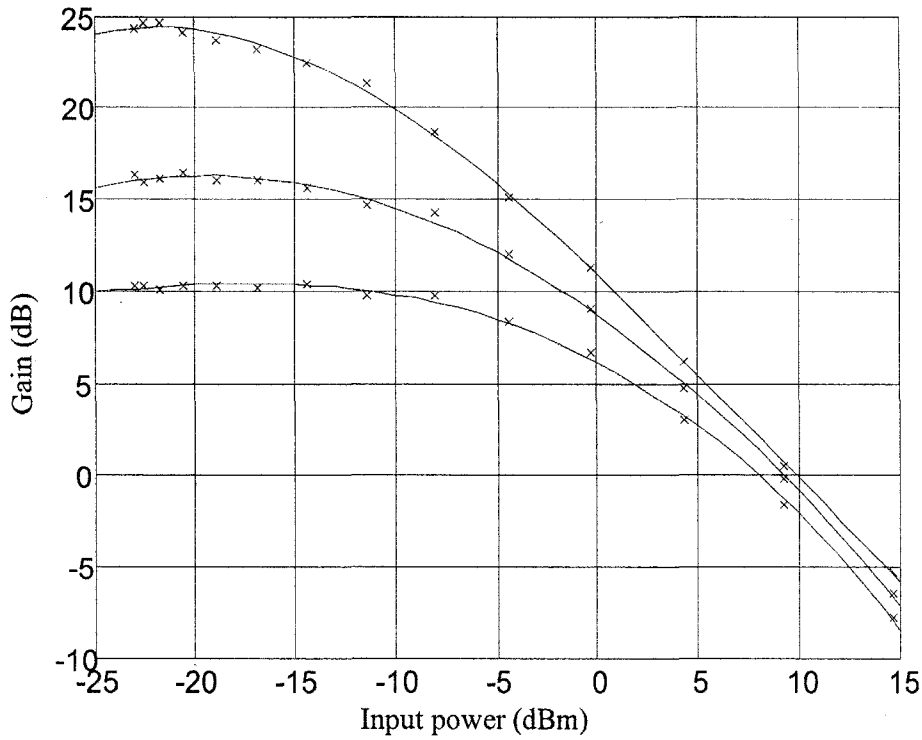


Figure 2-12: The graphs for gain vs. input power, from the bottom curve to the top, the cavity length equals to 0.085cm, 0.083cm, and 0.08cm respectively.

We can also explain this phenomenon from the mathematical approach based on (13) and (16). At the initial state, the carrier density $N$ can be approximately equaled to:

$$N_{initial} = \frac{I}{qwdL} \tag{45}$$

and the total gain is equal to:

$$G = G_0 e^{\Gamma g L} \tag{46}$$

where $G_0$ is a constant, $\Gamma$ is the confinement factor, $L$ is the cavity length, and $g$

is equal to equation (16):

$$g(z,t,\lambda_k) \cong \alpha(N(z,t)-N_{tr})[1-(\frac{\lambda_k-\lambda_p}{\lambda_w})^2]$$

substitute (16) and (45) into equation (46):

$$G_{initial} = G_0 e^{\Gamma\alpha(\frac{I}{qwdL}-N_{tr})[1-(\frac{\lambda_k-\lambda_p}{\lambda_w})^2]L} \tag{47}$$

For instance, if we reduce SOA's cavity length by half, the initial carrier density is doubled:

$$N_{initial} = \frac{2I}{qwdL} \tag{48}$$

and the total gain becomes:

$$G_{initial} = G_0 e^{\Gamma g_{initial}\frac{L}{2}} \tag{49}$$

We can substitute (16) into (49), and get to following:

$$G_{initial} = G_0 e^{\Gamma\alpha(N(z,t)-N_{tr})[1-(\frac{\lambda_k-\lambda_p}{\lambda_w})^2]\frac{L}{2}} \tag{50}$$

put (48) into (50):

$$G_{initial} = G_0 e^{\Gamma\alpha(\frac{2I}{qwdL}-N_{tr})[1-(\frac{\lambda_k-\lambda_p}{\lambda_w})^2]\frac{L}{2}} \tag{51}$$

and then we can simplify (51) even further:

$$G_{initial} = G_0 e^{\Gamma\alpha(\frac{2I}{qwdL} - N_{tr})[1-(\frac{\lambda_k-\lambda_p}{\lambda_w})^2]\frac{L}{2}}$$

$$G_{initial} = G_0 e^{\Gamma\alpha(\frac{I}{qwdL} - \frac{N_{tr}}{2})[1-(\frac{\lambda_k-\lambda_p}{\lambda_w})^2]L} \tag{52}$$

The $g$ is increased in (52), because the transparent carrier density $N_{tr}$ is reduced by half. Compared to (47), the initial gain in (52) is increased as well.

if we double SOA's cavity length, the initial carrier density is reduced by half:

$$N_{initial} = \frac{I}{2qwdL} \tag{53}$$

and the total gain becomes:

$$G_{initial} = G_0 e^{\Gamma g_{initial} 2L} \tag{54}$$

We can substitute (16) into (54), and get to following:

$$G_{initial} = G_0 e^{\Gamma\alpha(N(z,t)-N_{tr})[1-(\frac{\lambda_k-\lambda_p}{\lambda_w})^2]2L} \tag{55}$$

put (53) into (55):

$$G_{initial} = G_0 e^{\Gamma\alpha(\frac{I}{2qwdL} - N_{tr})[1-(\frac{\lambda_k-\lambda_p}{\lambda_w})^2]2L} \tag{56}$$

and then we can simplify (56) even further:

$$G_{initial} = G_0 e^{\Gamma\alpha(\frac{I}{2qwdL} - N_{tr})[1-(\frac{\lambda_k - \lambda_p}{\lambda_w})^2]2L}$$

$$G_{initial} = G_0 e^{\Gamma\alpha(\frac{I}{qwdL} - 2N_{tr})[1-(\frac{\lambda_k - \lambda_p}{\lambda_w})^2]L} \quad (57)$$

The $g$ is reduced in (57), because the transparent carrier density $N_{tr}$ is doubled. Compared to (47), the initial gain in (57) is reduced as well.

### 2.4.2 Gain Dependence on Injection Current

As the injection current $I$ is reduced, the gain goes down in a continuous way. This can be seen in the Figure 2-13. From the top to the bottom curves, the injection currents are 0.115A, 0.110A, and 0.105A respectively. When the current is lower than 0.105A, the gain becomes negative, and this can be treated as loss.

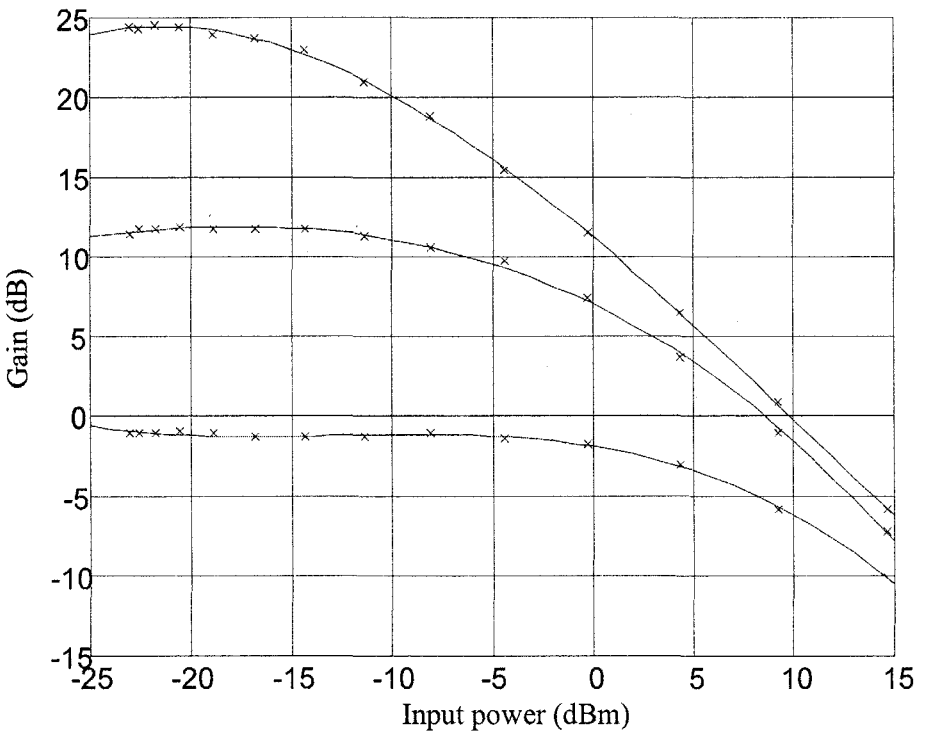


Figure 2-13: The graphs for gain vs. input power, from the top to the bottom curves, the injection current $I$ equals to 0.115A, 0.110A, and 0.105A respectively.

This effect can be explained by using (45) and (47):

$$N_{initial} = \frac{I}{qwdL}$$

$$G_{initial} = G_0 e^{\Gamma\alpha(\frac{I}{qwdL} - N_{tr})[1-(\frac{\lambda_h - \lambda_p}{\lambda_w})^2]L}$$

It's apparent that if injection current is decreased, both initial carrier density and gain will be reduced.

### 2.4.3 Gain Dependence on Confinement Factor

As the confinement factor $\Gamma$ is increased, the gain goes up in a continuous way. This can be seen in the Figure 2-14. From the top to the bottom curves, the confinement factors are 0.9, 0.85, and 0.8 respectively.

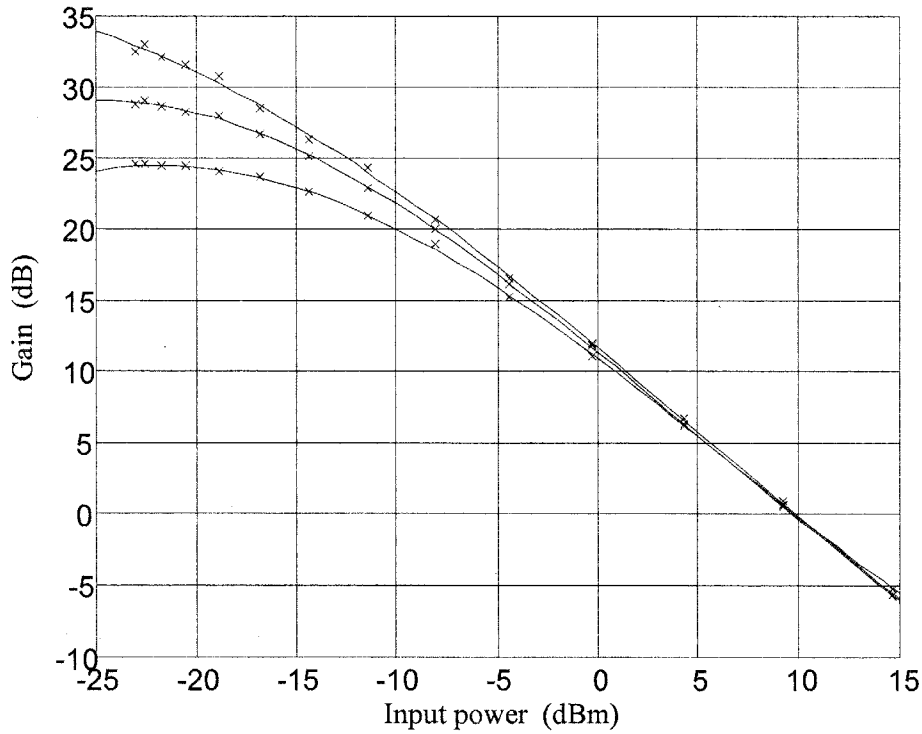


Figure 2-14: The graphs for gain vs. input power, from the top to the bottom curves, the confinement factor $\Gamma$ equals to 0.9, 0.85, and 0.8 respectively.

This effect can be explained from theoretical aspect. Confinement factor $\Gamma$ measures how much the optical field cross-sectional distribution is overlapped with the gain region. With high confinement factor, the gain region becomes more effective, and more photons will experience the gain in their propagation along the cavity, hence we obtain higher gain.

### 2.4.4 Gain Dependence on SRH Recombination Coefficient

As the SRH recombination coefficient $A$ is increased, the gain goes down in a continuous way. This can be seen in the Figure 2-15. From the top to the bottom curves, the SRH recombination coefficients are $2.7\times10^{8}\ /s$, $2.8\times10^{8}\ /s$, and $2.9\times10^{8}\ /s$ respectively.

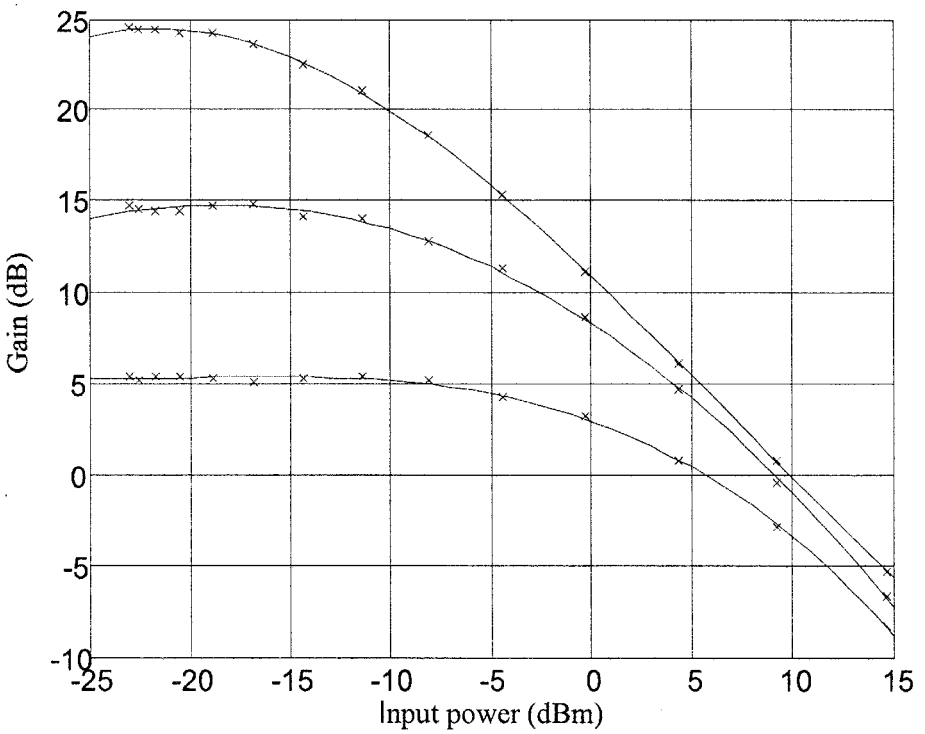


Figure 2-15: The graphs for gain vs. input power, from the top to the bottom curves, the SRH recombination coefficients are $2.7\times10^{8}\ /s$, $2.8\times10^{8}\ /s$, $2.9\times10^{8}\ /s$ respectively.

This phenomenon can be explained as following: from the theoretical point of view, SRH recombination coefficient $A$ is the carrier non-radiative recombination rate (its inverse is the carrier lifetime). As $A$ increases, more carriers are consumed

per unit time through the non-radiative process that doesn't emit any photon. Under a fixed bias current, the carrier injection rate is fixed, if the carrier consumption rate on the non-radiative process is high, the available carriers on radiative process must be less. Therefore, we have lower stimulated emission rate, hence we have less gain.

### 2.4.5 Gain Dependence on Modal Loss

As the modal loss $a_s$ is increased, the gain goes down in a continuous way. This can be seen in the Figure 2-16. From the top to the bottom curves, the modal loss is 43/cm, 0.63/cm, and 6=83/cm, respectively.

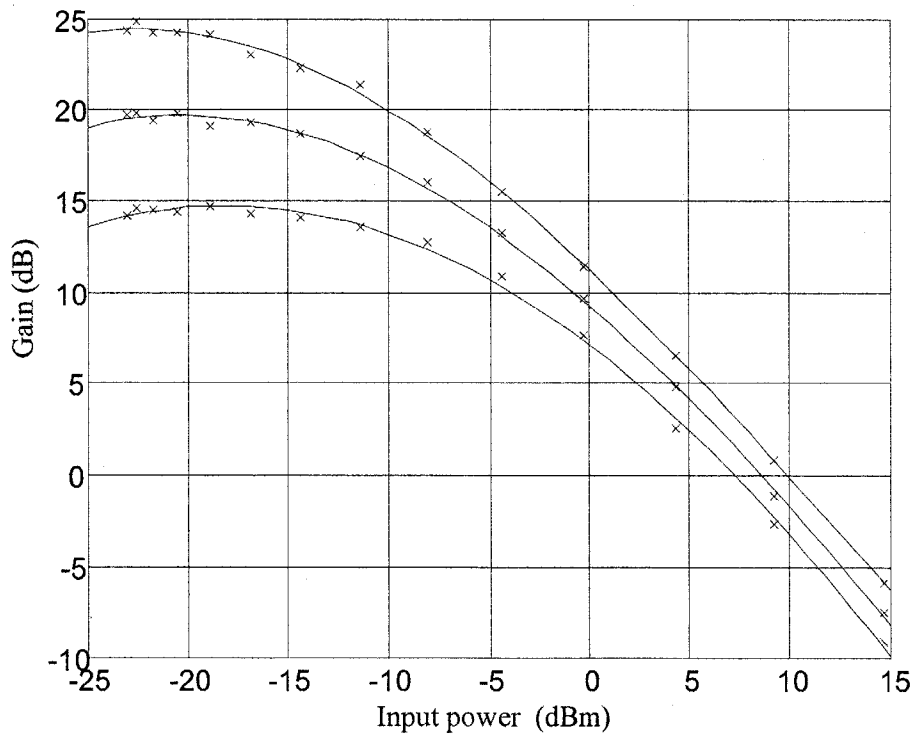


Figure 2-16: The graphs for gain vs. input power, from the top to the bottom curves the modal loss are 43/cm, 0.63/cm, and 6=83/cm, respectively.

This occurrence is quite obvious as the net gain comes from the gain minus the optical loss. The gain comes from the interband electron-hole recombination. The optical loss comes from the free electron absorption in the cladding area outside of the active region and from the optical scattering at waveguide boundaries. As the modal loss $a_s$ increases, the optical loss increases, both material gain and net gain will be reduced.

### 2.4.6 The Gain Dependence on Transparent Carrier Density

As the transparent carrier density $N_{tr}$ is increased, the gain goes down in a continuous way. This can be seen in the Figure 2-17. From the top to the bottom curves, the transparent carrier density is $1\times10^{18}/cm^3$ , $1.02\times10^{18}/cm^3$ , and $1.04\times10^{18}/cm^3$, respectively.

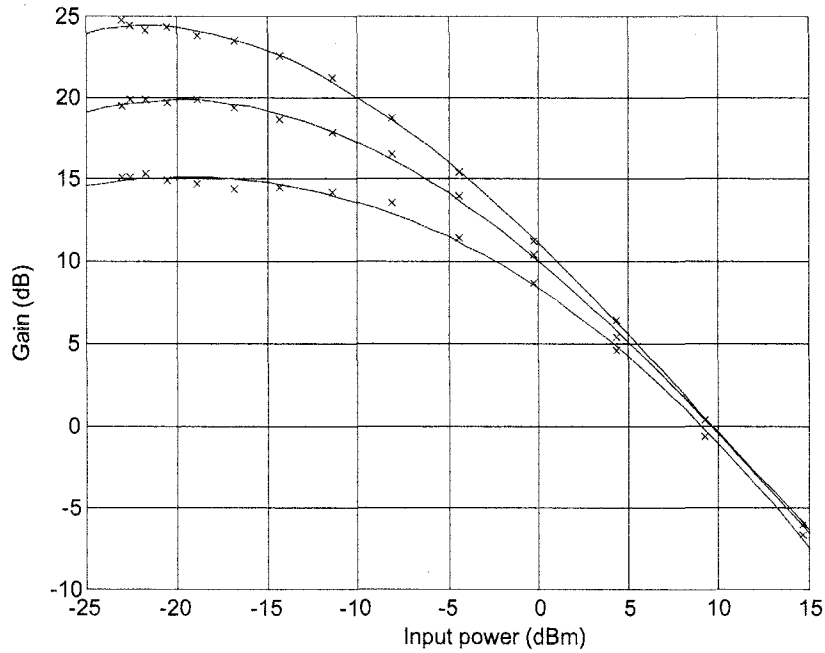


Figure 2-17: The graphs for gain vs. input power, from the top to the bottom curves, transparent carrier densities are $1\times10^{18}/cm^3$ , $1.02\times10^{18}/cm^3$ , and $1.04\times10^{18}/cm^3$, respectively.

The above phenomenon can be explained as following: the material gain is proportional to the injected carrier density minus the transparent carrier density. For a fixed injection current, the total injected carrier is also fixed. If the transparent carrier density is higher, the material gain is certainly smaller due to the reduction on the net injection. We can also take the mathematical approach, based on (16) and (46).

$$g(z,t,\lambda_k) \cong \alpha(N(z,t) - N_{tr})[1 - (\frac{\lambda_k - \lambda_p}{\lambda_w})^2]$$

as the $N_{tr}$ increases, the material gain $g$ decreases. Following (46):

$$G = G_0 e^{\Gamma g L}$$

the total gain $G$ will be decreased due to the increment of transparent carrier density $N_{tr}$.

# Chapter 3 Modeling of PIN Photodetector

## 3.1 Review of PIN Photodetector

In the case of photodetector, a photon with an energy $\hbar w > E_g$, the band gap energy, can release an electron from the valence band. In other words, a photon is annihilated to create an electron-hole pair. To facilitate photon absorption, we need more electrons in the valence band; this is achieved by reverse biasing P-N junction.

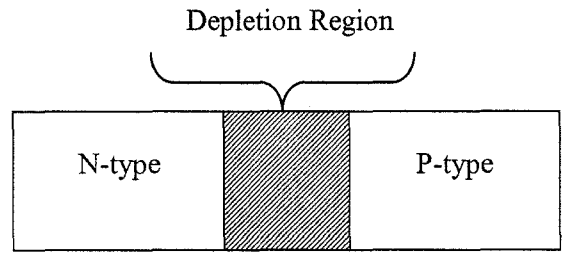


Figure 3-1: A schematic view of P-N junction.

A N-type material has free electrons moving around to in the lattice; similarly, a P-type material has holes. When a P-N junction is formed, electrons from n side diffuse across from the junction, and combine with holes from the other side. Similarly, holes from P-side also diffuse to the n-side, and combine with electrons. As a result, the junction area has no mobile carriers, since electrons and holes are locked into a covalent structure. This region is called the depletion region.

When an external battery is connected to the P-N junction, with its positive terminal connected to the N-type material and its negative terminal connected to the P-type material, the junction is said to be reverse biased. As a result of reverse biasing, the width of the depletion region will increase on both N-side and P-side.

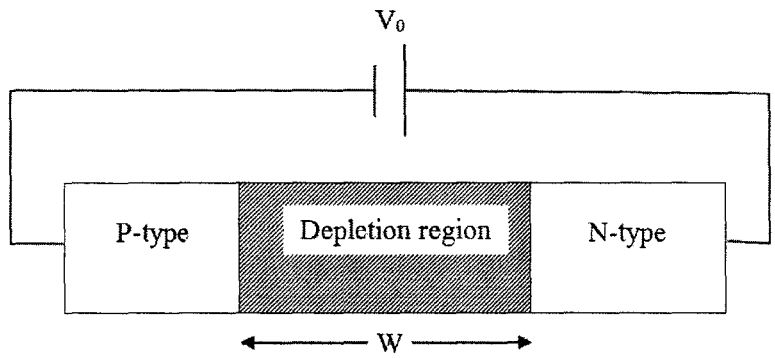


Figure 3-2: A P-N junction under reverse bias.

The wider depletion region could be beneficial, since the amount of photons absorption can be enhanced.

The working procedures of the reverse-biased P-N photodetector can be illustrated as Figure 3-2. The working procedures are [4]:

1. P-N junction is illuminated on the P-side;
2. Electron- hole pairs are created through absorption;
3. Electrons and holes generated accelerate inside depletion region in opposite direction due to the large build-in electric field;
4. Electrons and holes diffuse outside the depletion region.

A reverse biased P-N junction consists of a region known as depletion region that is devoid of free charge carriers. When light falls on one side of a P-N junction, electrons absorb light and make a transition from valence band to conduction band, if the photon energy $\hbar w$ is greater than or equal to the band gape energy $E_g$. This is illustrated by Figure 3-3.

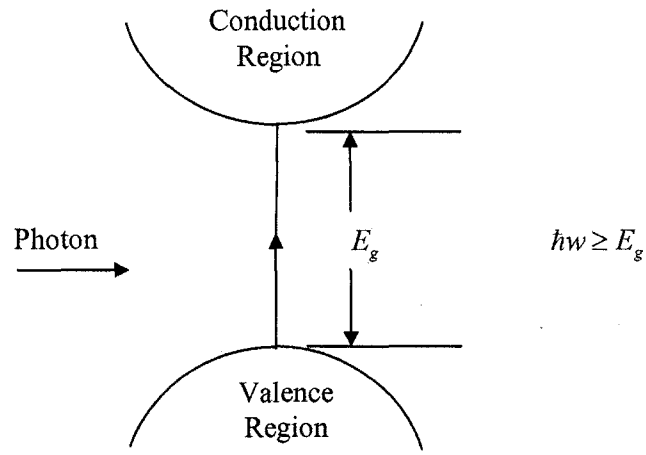


Figure 3-3: The schematic view of photon absorption between conduction band and valence band.

This means electrons could move freely in the lattice. The absence of electrons in the valence band leads to a hole. Thus, if a photon is absorbed, an electron-hole pair is created. The electrons and holes generated inside the depletion region accelerate in the opposite directions due to the reverse bias. This gives rise of a current flow in an external circuit, and this current flow is known as photocurrent.

Let the optical power incident on one side of the P-N junction be $P_0$. If the facets of semiconductor slab have anti-reflection coating, the incident optical power will not be reflected backwards.

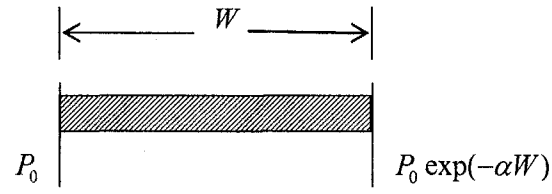


Figure 3-4: The semiconductor slab with anti-reflection coating on the facets.

The power transmitted through the depletion region of width $W$ is

$$P_{tr} = P_0 \exp(-\alpha W) \tag{58}$$

Where $\alpha$ is absorption coefficient.

Optical power decreases exponentially due to the absorption. The optical power absorbed within the depletion region could be expressed as:

$$P_{abs} = P_0 - P_{tr} = P_0(1 - \exp(-\alpha W)) \tag{59}$$

where $P_0$ is the optical input power at the left side of the depletion region, $P_{tr}$ is the output optical power at the right side of the depletion region, $W$ is the width of the depletion region.

We know that: $\frac{Optical\ \ Energy}{\hbar w} = Number\ of\ \ photons$ (60)

Number of photons per unit time= $\frac{Energy}{time \bullet \hbar w} = \frac{Power}{\hbar w}$ (61)

Number of photon absorbed per unit time= $\frac{P_{abs}}{\hbar w}$ (62)

If a photon is absorbed, an electron-hole pair is generated. Therefore, the number of electrons generated per unit time is:

$$\frac{N_e}{T} = \frac{P_{abs}}{\hbar w} \tag{63}$$

$N_e$: Number of electrons generated

$T$: Time interval

Since generated electrical current is:

$$I = \frac{N_e q}{T} \tag{64}$$

$q$: electron charge

We can substitute (59) into (64):

$$I = \frac{P_{abs} q}{\hbar w} = \frac{P_0(1-\exp(-\alpha W))q}{\hbar w} \tag{65}$$

The quantum efficiency is equal to:

$$\eta = \frac{electron\ generated\ rate}{photon\ incident\ rate} \tag{66}$$

Electron generated rate is equal to: $\frac{N_e}{T} = \frac{I}{q}$ (67)

Number of photons incident in one side of p-n junction per unit time is equal to photon incident rate:

$$\text{Photon incident rate} = \frac{P_0}{\hbar w} \tag{68}$$

$$\eta = \frac{\frac{I}{q}}{\frac{P_0}{\hbar w}} \tag{69}$$

We can obtain $\eta = 1 - \exp(-\alpha W)$. If $W$ is large, $\exp(-\alpha W) \approx 0$ and $\eta \approx 1$. In this case, most of photons incident photons are absorbed. Therefore, quantum efficiency is nearly 100%. When $W$ is small, $\exp(-\alpha W) \approx 1 - \alpha W + O(W^2)$

For practical problem, one would like to know how much current is generated for the given incident power. Therefore, responsivity of a photodetector is defined as

$$R = \frac{I}{P_0} \tag{70}$$

It follows that $R = \frac{\eta q}{\hbar w}$ and $I = (\frac{\eta q}{\hbar w}) P_0$.

The bandwidth of a photodetector is determined by the speed with which it responds to variation in the incident optical power. If the incident optical power changes abruptly, as shown in the Figure 3-5, the electrical current builds up gradually.

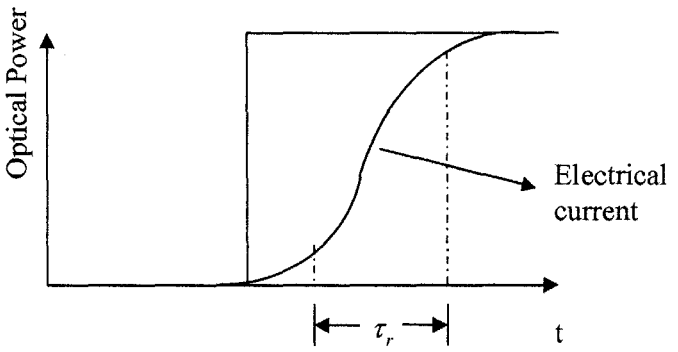


Figure 3-5: The electrical current builds up gradually, when optical power changes abruptly.

The rise time $\tau_r$ is defined as the time over which the current builds up from 10% to 90% of its final value and it given by:

$$\tau_r = (\ln 9)\bullet(\tau_{tr} + \tau_{RC}) \tag{71}$$

Where $\tau_{tr}$ is transit time, and $\tau_{RC}$ is the time constant of an equivalent RC circuit.

Transit time $\tau_{tr}$ is the time taken by an electron to traverse the depletion region. If the $W$ is the width of the depletion region and $v_d$ is the drifty velocity, the transit time is:

$$\tau_{tr} = \frac{W}{v_d} \tag{72}$$

$$\tau_{RC} = (R_L + R_S)C_P \tag{73}$$

where $R_L$ is the external load resistance, $R_S$ is the internal resistance, $C_P$ is the parasitic capacitance [4]..

For a photodetector, the bandwidth $\Delta f$ is given by: $\Delta f = \frac{1}{2\pi(\tau_{tr} + \tau_{RC})}$ (74)

If the width of the depletion layer is large, we know that quantum efficiency increases, because more photons can be absorbed over a wider region. However, the transit time $\tau_{tr}$ increases with the width of the depletion layer. Therefore, bandwidth $\Delta f$ decreases. So, there is a trade-off between efficiency and bandwidth.

In [4], it shows the wavelength dependence of the absorption coefficient $\alpha$ for several semiconductor materials. The wavelength $\lambda_c$ at which the absorption coefficient $\alpha$ becomes zero is called the cut-off wavelength. If the incident wavelength $\lambda$ is greater than the $\lambda_c$, the photodetector will not absorb light. This is because $\lambda > \lambda_c \Rightarrow$ *frequency* $f < f_c = \frac{E_g}{h}$, where $E_g$ is the band gap energy.

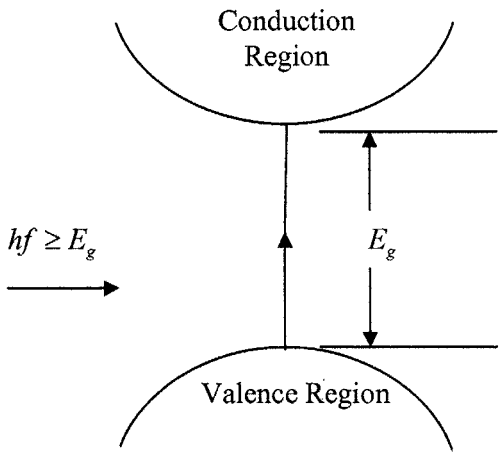


Figure 3-6: The photon can not be absorbed due to inefficient energy.

In this case, energy of the photon will not be adequate to excite an electron to conduction band, so such a photon will not be absorbed.

To increase the quantum efficiency, it is desirable to increase the width $W$ of the depletion region. This can be done by increasing a layer of undoped or slightly doped intrinsic semiconductor material between the P-N junction, such a photodetector is called PIN photodetector. In this structure, the depletion region extends throughout the I-region, and its width $W$ can be controlled by changing the middle i-layer thickness. The structure and electrical field of it is illustrated in Figure 3-7. The I-layer has high resistance, so that most of the voltage drops across it, and there is large electric field within the layer. As a result, depletion region extends through the I-layer, and its width $W$ could be controlled by changing the thickness of the I- layer.

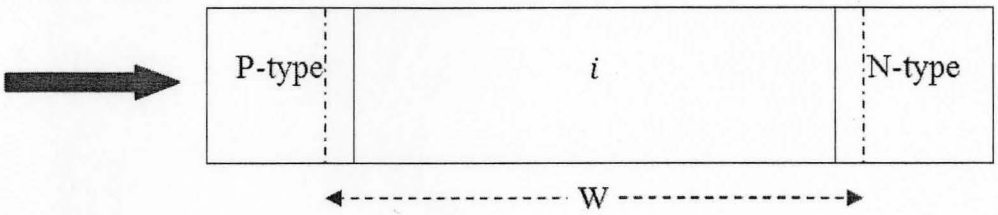


Figure 3-7: A PIN photodetector that the thickness of depletion region is W.

The optimum choice of $W$ depends on a compromise between speed, i.e. bandwidth and efficiency.

1. Quantum efficiency increases when $W$ increases, up to near 100%;
2. Drift time (the most significant time for PIN) increases when $W$ increases, this lowers the speed.

## 3.2 Simulation of PIN Photodetector

In our system, the essential functionality of PIN photodetector is converting optical input power into electrical current through photoelectrical effect. We have discussed this property in the previous sections. In order to simplify our simulation process, we did not take the conventional PIN modeling approach and some phenomena are omitted for simplification. However, the much simpler current approach has been taken.

The input optical power of PIN photodetector is $P_0$, the responsivity of PIN photodetector is $R$, and the current generated by PIN photodetector is $I_p$. A fraction of the contribution to the electric current is from a stream of electrons generated at

random times. This leads to a noisy component in the current. When an optical signal of power $P_0$ falls on the photodetector, the current can be written as:

$$I(t) = I_p + \tilde{I}_s(t) \tag{75}$$

$I_p = RP_0$ and $I_p$ is the deterministic part of the current.

$\tilde{I}_s(t)$ is the noise component of the current due to short noise.

Note that in the conventional PIN modeling, there are two kinds of noise currents involved, one is short noise current and the other is thermal noise current. Since we did not take thermal effect into our consideration, we omitted the thermal noise current in the modeling.

The short noise current $\tilde{I}_s(t)$ is a random variable with zero mean.

$$E\left[\tilde{I}_s(t)\right] = 0,\ E \text{ stands for expectations} \tag{76}$$

The variance of short noise current is $\sigma_S^2 = 2qI_P\Delta f$, $\sigma_S$ is the standard deviation. The detailed derivations for short noise current variance $\sigma_S^2$ can be found in Chapter. 5.

Since both mean and variance of short noise current can be derived, we can model $\tilde{I}_s(t)$ through a Gaussian distributed random number generator with $E\left[\tilde{I}_s(t)\right] = 0$ and $\sigma_S^2 = 2qI_P\Delta f$.

A simple PIN structure is used for simulation, which is illustrated in Figure. 3-8:

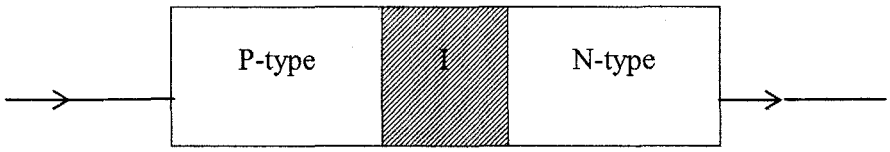


Figure 3-8: A simplified structure of PIN photodetector.

The following table lists all the parameters we used during the PIN photodetector simulation.

| variable | Physical meaning | Type | Dimension | Value |
|---|---|---|---|---|
| $R$ | responsivity | constant | dimensionless | 0.7 |
| $q$ | Electron charge | constant | Coulomb | 1.6e-19 |
| $\Delta f$ | The bandwidth | constant | Hz | 1.8e9 |
| $\tilde{I}_s(t)$ | Short noise current | Intermediate variable | Ampere (A) | |
| $P_0$ | Input optical power of PIN photodetector | Intermediate variable | Watt | |
| $\sigma_S^2$ | Variance of short noise current | Intermediate variable | dimensionless | |
| $I_p$ | Deterministic part of the current. | Intermediate variable | Ampere (A) | |

Table 3: Parameters for the simulation of PIN photodetector.

After the incident optical signal passes through SOA, as shown in Figure 2-6 and Figure 2-8, the optical signal power will be transformed to current by PIN

photodetector through photoelectrical effect. This is shown in Figure 3-9 and Figure 3-10 respectively, which includes both deterministic current and short noise current.

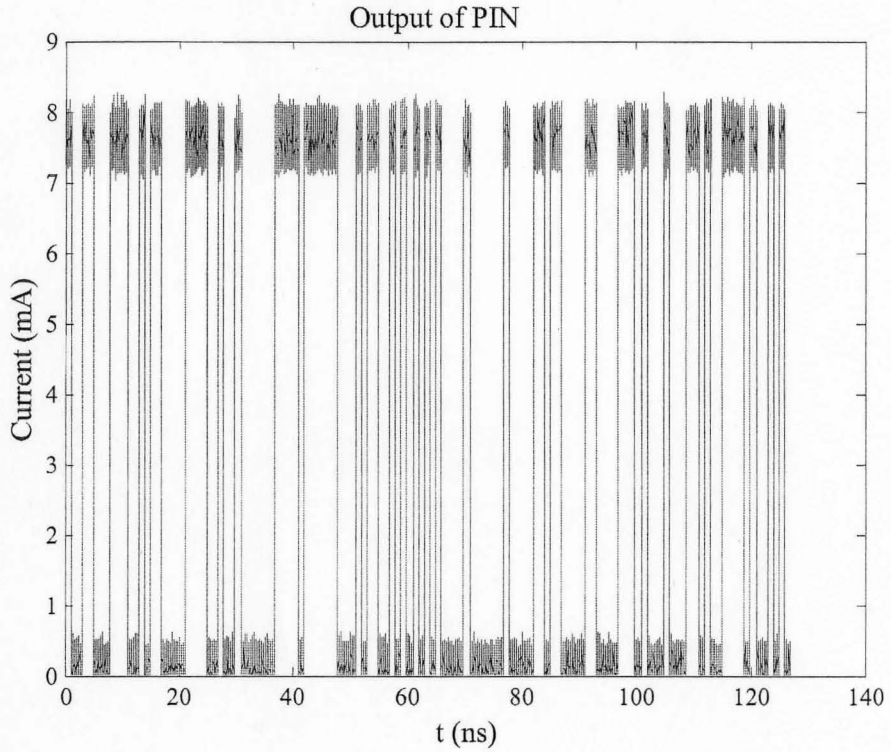


Figure 3-9: The output current from PIN photodetector, when the output power from SOA is 11 mW.

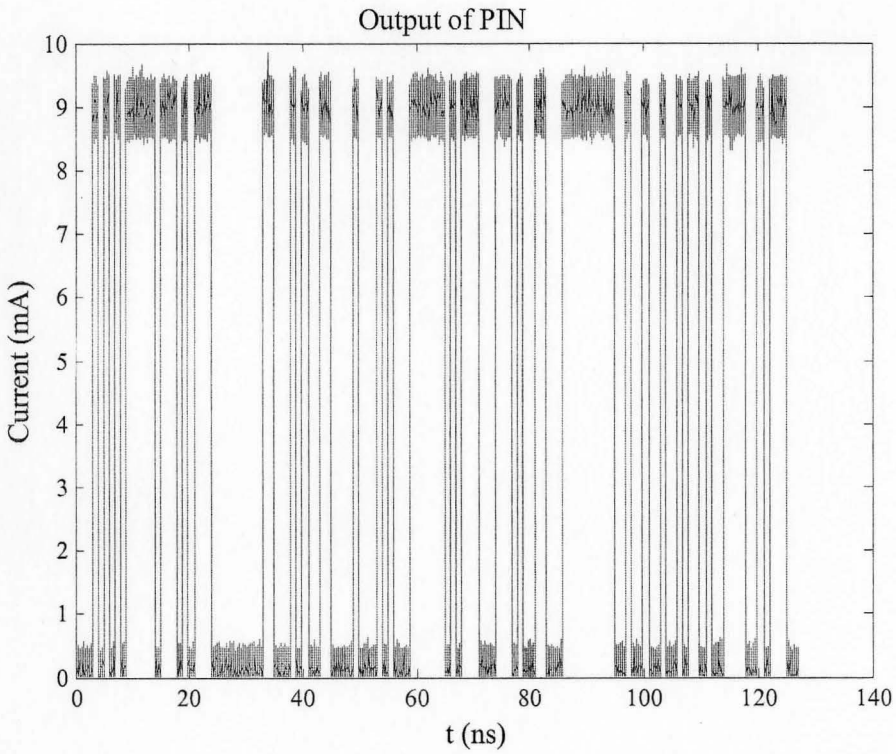


Figure 3-10: The output current from PIN photodetector, when the output power from SOA is 13 mW.

# Chapter 4 Modeling of Low Pass Filte

## 4.1 Review of Ideal Low Pass Filter

A low-pass filter (LPF) is a filter that passes low-frequency signals but attenuates (reduces the amplitude of) signals with frequencies higher than the cutoff frequency. An ideal LPF completely eliminated all frequencies above the cut-off frequency while passing those below unchanged.

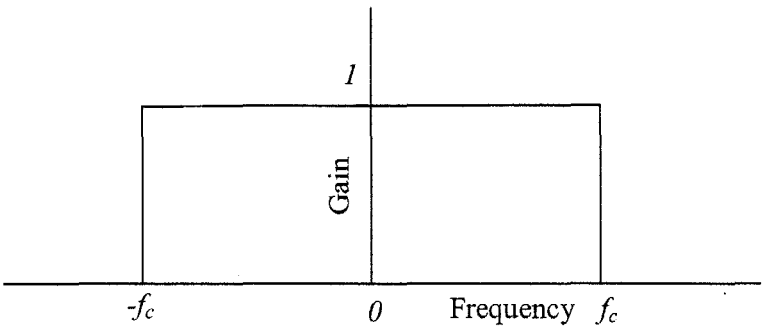


Figure 4-1: The frequency response of ideal low-pass filter. The horizontal axis is frequency and the vertical axis is gain.

The following is the transfer function for the ideal LPF in the frequency domain.

$$H_{ideal}(f) = \begin{cases} 1 & |f| \le f_c \\ 0 & |f| > f_c \end{cases} \tag{77}$$

Consider an ideal LPF, depicted in Figure 4-1. The ideal LPF is characterized by a gain of 1 for all frequencies below some cut-off frequency $f_c$ in normalized Hz, and a gain of 0 for all higher frequencies. The frequency response of ideal LPF is governed by (77). The impulse response of the ideal LPF is calculated as follow:

$$h_{ideal}(n) \triangleq DTFTn^{-1}\left[H_{ideal}(f)\right]$$

$$\triangleq \frac{1}{2\pi}\int_{-\pi}^{\pi} dwe^{jwn}\begin{cases}1 & |w| \le w_c \\ 0 & |w| > w_c\end{cases}$$

$$\triangleq \frac{1}{2\pi}\int_{-w_c}^{w_c} e^{jwn}dw$$

$$\triangleq \frac{1}{2\pi jn}(e^{jw_c n} - e^{-jw_c n})$$

$$\triangleq \frac{\sin(w_c n)}{\pi n} \qquad (78)$$

Where $w_c = 2\pi f_c$ is the normalized cut-off frequency in radians per sample.

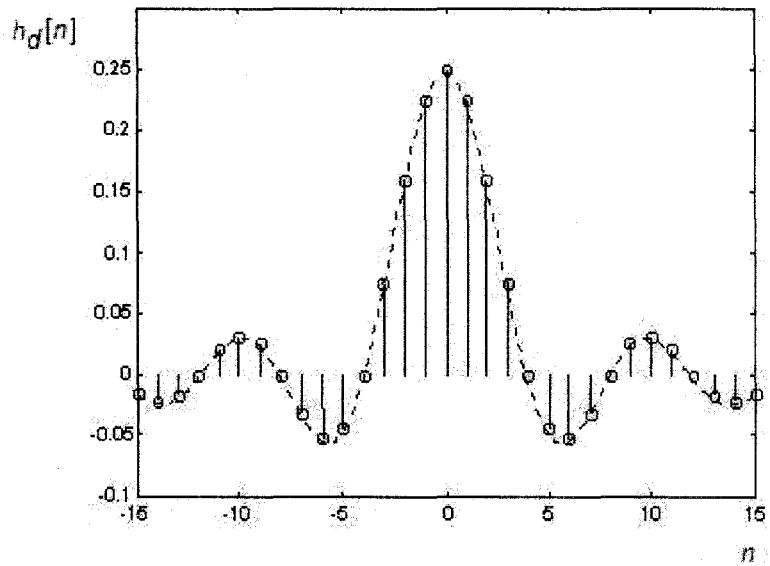


Figure 4-2: The impulse response of ideal low pass filter.

Unfortunately, we cannot implement the ideal LPF in practice because its impulse response is infinitely long in time. Also note that it is non-causal. It cannot be shifted to make it causal because the impulse response extends all the way to time $-\infty$. It is

clear we will have to accept some sort of compromise in the design of any practical LPF. Practical LPFs for real-time applications approximate the ideal filter by truncating and windowing the infinite impulse response to make a finite impulse response.

## 4.2 Low Pass Filter Realization in Time-Domain through IIR-DSP

Many applications in signal processing or communication field require us to deal with the incoming signals in real-time; namely, the signal must be processed sample by sample in time domain rather than frame (a group of samples) by frame. A typical example is to build a digital filter in a way that the fast-varying components (high frequency components) in the signal will be dropped while the slow-varying components (low frequency components) will be reserved in their original form, i.e., we want to let the signal pass through a (frequency domain) LPF. Our problem can be illustrated as Figure. 4-3,

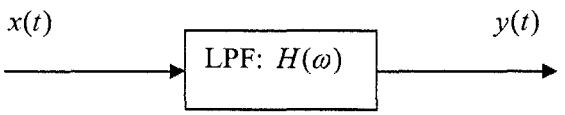


Figure 4-3: The schematic view of traditional LPF system.

where $x(t)$ denotes the incoming signal to be processed, $y(t)$ denotes the demanded signal after the processing, $t$ is the time variable, $H(\omega)$ is a given frequency domain system transfer function which, in our particularly problem, can be specified by, for example, a standard 1$^{st}$ order low-pass filter:

$$H(\omega) = \frac{\omega_c}{\omega_c + j\omega} \tag{79}$$

where $\omega = 2\pi f$ is the angle frequency variable, $\omega_c = 2\pi f_c$ is known as the cut-off angle frequency, as shown in Figure 4-4.

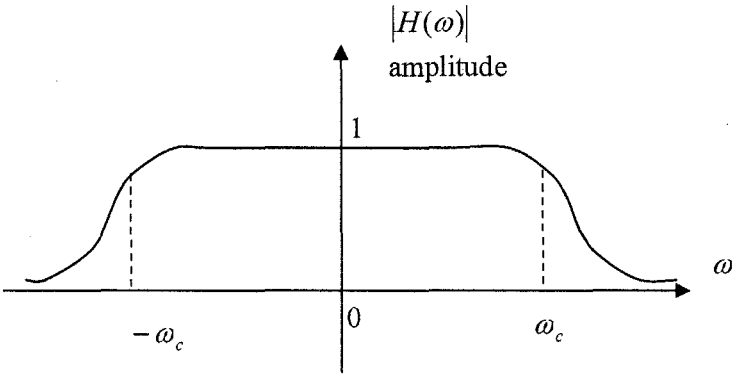


Figure 4-4: The frequency response of non-ideal LPF. The horizontal axis is angular frequency and the vertical axis is gain.

It is trivial to build an algorithm to compute $y(t)$ for specified $H(\omega)$ and given $x(t)$. If the "real-time" constraint is removed, as it is well-known that:

$$y(t) = F^{-1}\{H(\omega)F[x(t)]\} \tag{80}$$

where $F$ and $F^{-1}$ denote the Fourier and inverse Fourier transforms, respectively. However, this algorithm doesn't apply to our problem, as we have to wait until enough samples in time domain are collected to form a frame before the Fourier transform can be performed.

We also have a time domain direct convolving algorithm derived from (80):

$$y(t) = \int_0^{t} h(\tau)x(t-\tau)d\tau + \int_{0+}^{t-} g(\tau)y(t-\tau)d\tau \tag{81}$$

where $h(t)$ and $g(t)$ are both related to the inverse Fourier transform of $H(\omega)$ ,known as the open loop and feedback impulse responses of the system, respectively. Here we also assume that the incoming signal $x(t)$ starts from $t = 0$. This algorithm is causal hence fits our real-time requirement as it only employs the current sample, the previous samples and the previous responses. Any future sample, any current or future responses at time $> t$ is not used.

Noting that we are actually dealing with a discrete signal with a uniform time domain sampling interval $\Delta$, (81) can only be implemented in the following form:

$$y(t) = \sum_{k=0}^{M-1} h_k x(t-k\Delta) + \sum_{l=1}^{L} g_l y(t-l\Delta) \tag{82}$$

Here is our problem: how to compute these $h_k$'s and $g_l$'s,

$k = 0,1,2,...,M-1, l = 1,2,...,L, L \le M-1$.

Perform Fourier transform on both sides of (82) yields:

$$\begin{aligned} F[y(t)] &= \sum_{k=0}^{M-1} h_k F[x(t-k\Delta)] + \sum_{l=1}^{L} g_l F[y(t-l\Delta)] \\ &= \sum_{k=0}^{M-1} h_k e^{jk\Delta\omega} F[x(t)] + \sum_{l=1}^{L} g_l e^{jl\Delta\omega} F[y(t)] \end{aligned} \tag{83}$$

Or:

$$F[y(t)] = \frac{\sum_{k=0}^{M-1} h_k e^{jk\Delta\omega}}{1 - \sum_{l=1}^{L} g_l e^{jl\Delta\omega}} F[x(t)] \tag{84}$$

Taking inverse Fourier transform on both sides of (84) yields:

$$y(t) = F^{-1}\{\frac{\sum_{k=0}^{M-1} h_k e^{jk\Delta\omega}}{1 - \sum_{l=1}^{L} g_l e^{jl\Delta\omega}} F[x(t)]\} \tag{85}$$

By comparing (80) with (85), we have:

$$H(\omega) = \frac{\sum_{k=0}^{M-1} h_k e^{jk\Delta\omega}}{1 - \sum_{l=1}^{L} g_l e^{jl\Delta\omega}} \tag{86}$$

Obviously, we are now looking for a best fit between the $H(\omega)$'s defined by the target form (79) and our model (86). With such extracted $h_k$'s and $g_l$'s, (82) can readily be used for the computation of $y(t)$, or say, to implement the digital low-pass digital filter to obtain the desired signal.

### 4.2.1 Approaches

Conventional approaches based on FFT/IFFT are far from ideal. On one hand, the FFT/IFFT is constrained by the "real-time" requirement and thus is not applicable to our problem. On the other hand, a large number of nonzero $h_k$'s and $g_l$'s is usually involved, leading to too much computation effort on (82) and complicating the implementation.

Therefore, a sophisticated fitting or optimization algorithm is highly demanded in the extracting of $h_k$'s and $g_l$'s, namely, the weighting coefficients in (82). To be more specific, extracting the appropriate $h_k$'s and $g_l$'s that enable our model to agree as closely as possible with the target form of the filter is a nonlinear least-squares problem, which can be formulated as seeking for the global minimizer of the following least-squares function:

$$\varepsilon(h_0, h_1, h_2, \ldots, h_{M-1}, g_1, g_2, \ldots, g_L) = \sum_n \left| H(\omega_n) - \frac{\sum_{k=0}^{M-1} h_k e^{jk\Delta\omega_n}}{1 - \sum_{l=1}^{L} g_l e^{jl\Delta\omega_n}} \right|^2 \tag{87}$$

where $H(\omega)$ is given in (79), $M$ and $L \le M-1$ are given integers, $\omega_n = n\Delta_\omega$, $\Delta$ and $\Delta_\omega$ are given real numbers known as the sampling intervals in time domain and frequency domain, respectively, $n \in [-N, N]$, $N \ge M + L$, $h_k$'s and $g_l$'s are complex numbers.

## 4.3 Simulation of Low Pass Filter

The frequency response of LPF and phase of LPF are shown in Figure 4-5, and Figure 4-6 respectively.

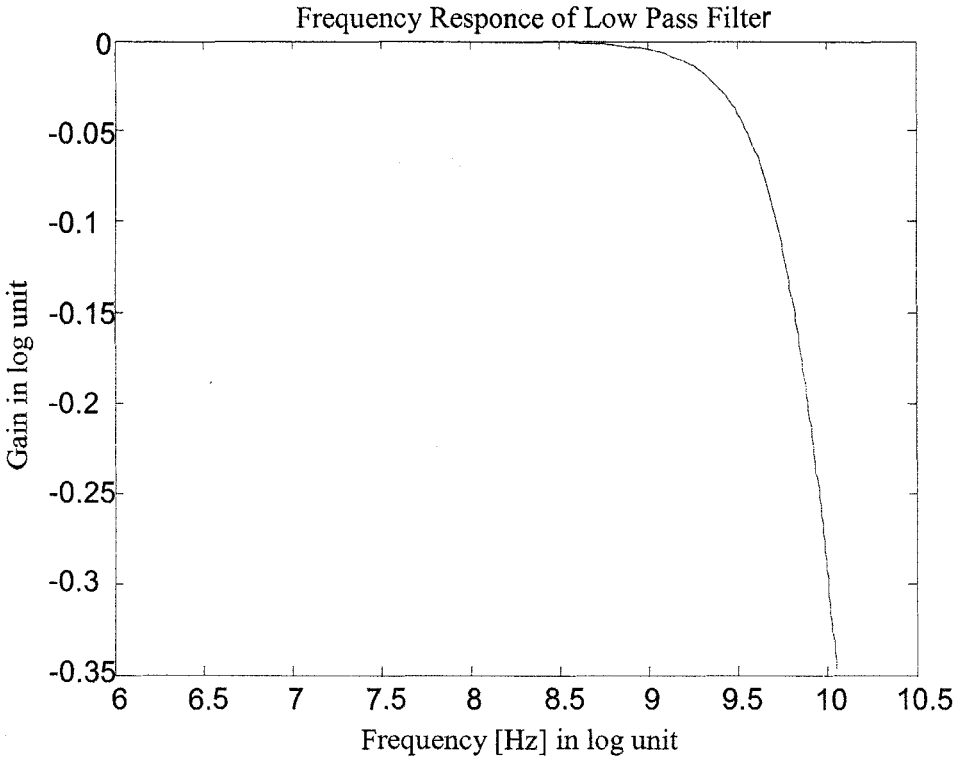


Figure 4-5: The frequency response of low pass filter.

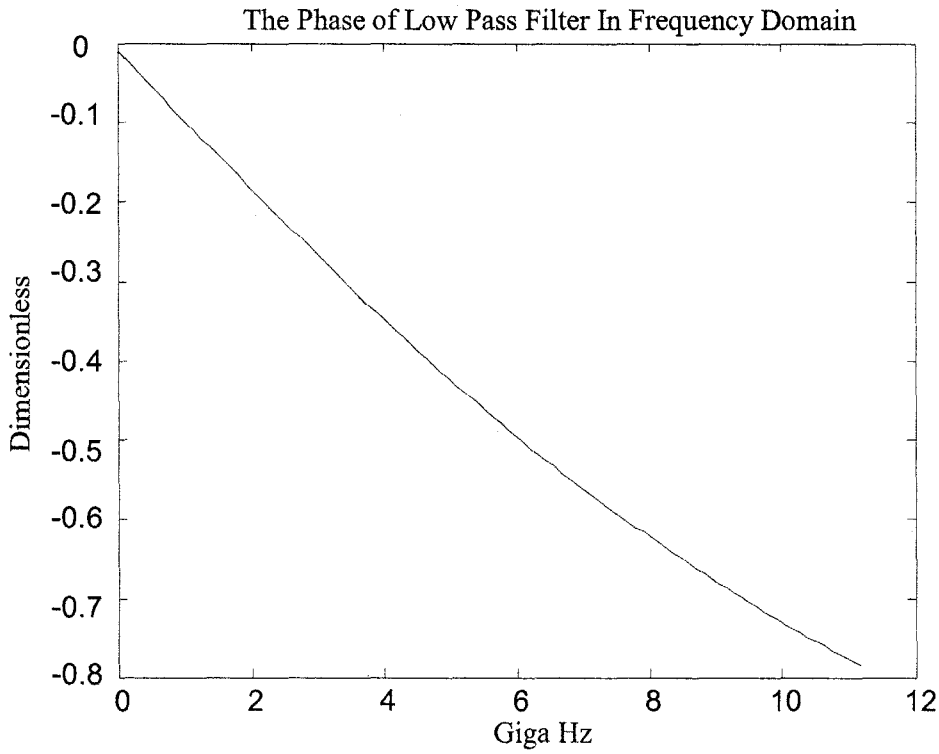


Figure 4-6: The phase of low pass filter in frequency domain.

In order to reduce the short noise in the current to the minimum level, as shown in Figure 3-9 and Figure 3-10, we pass the PIN photodetector current through LPF. The output current from LPF is shown in Figure 4-7 and Figure 4-8 respectively.

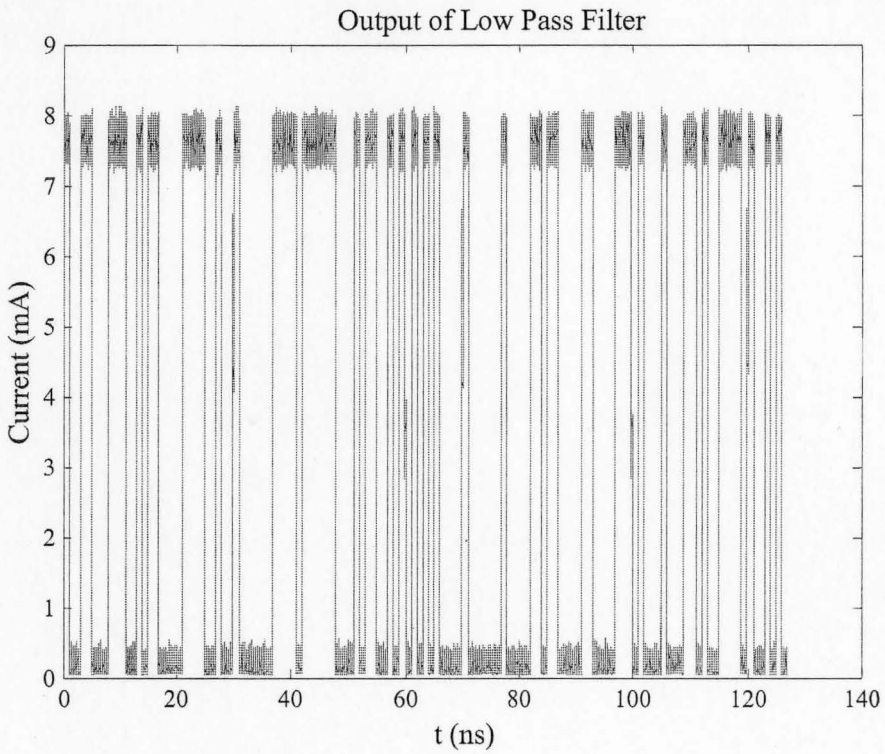


Figure 4-7: The output current from low pass filter, which corresponds to PIN current in the Figure 3-12.

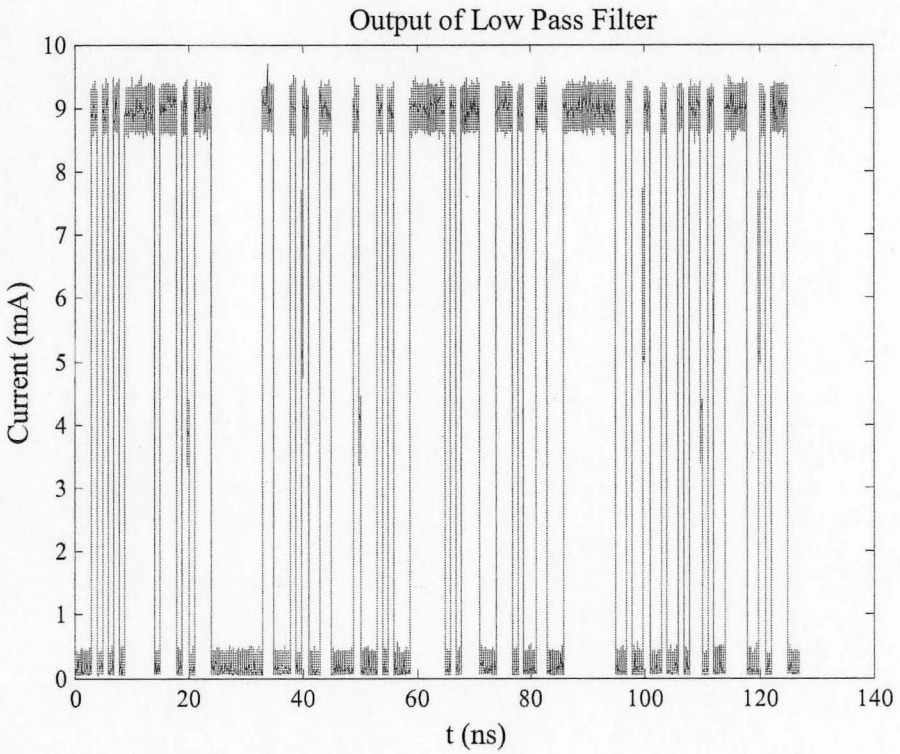


Figure 4-8: The output current from low pass filter, which corresponds to PIN current in the Figure 3-13.

# Chapter 5 Modeling and Simulation of Saturable Optical Receiver for FTTH Networks

So far we have been only considering photonic components, such as semiconductor optical amplifier (SOA), PIN photodetector, and low pass filter. In this chapter, we will consider both tradition optical receiver and proposed saturable optical receiver (SOR) for FTTH network.

## 5.1 Review on Optical Receiver

### 5.1.1 Theoretical Model of Optical Receiver

The main component of an optical receiver is a photodetector that converts light into electricity through the photoelectric effect. The photodetector is typically a semiconductor-based photodetector, such as PIN photodetector.

The PIN photodetector is typically coupled with a amplifier to produce an amplified signal from the incoming optical signal, which may be attenuated and distorted by passing through the channel. Further signal processing such as clock recovery from data by a phase-locked loop may also be applied before the data is passed on.

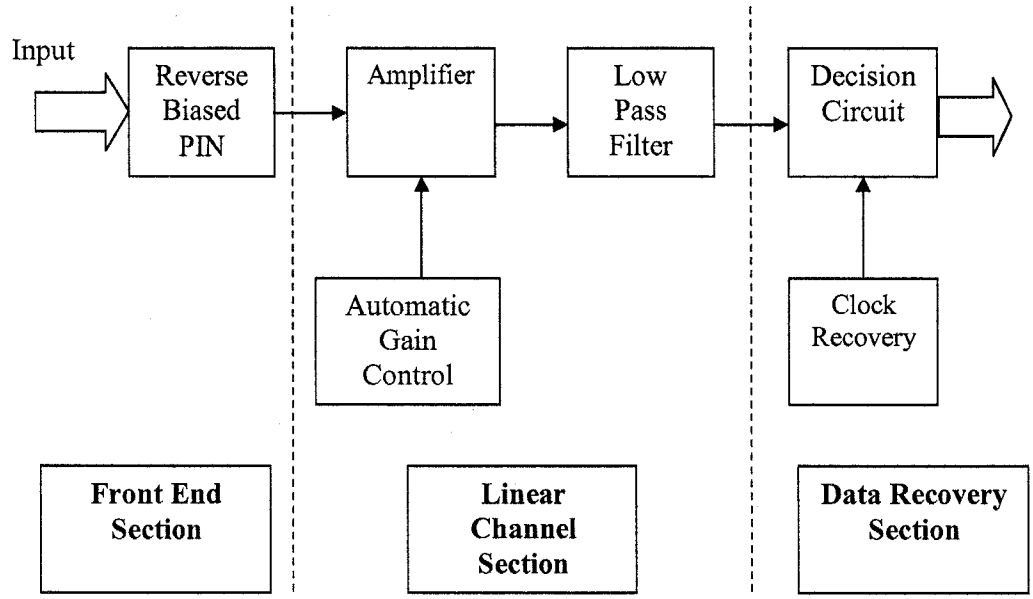


Figure 5-1: Block diagram of a theoretical optical receiver.

The Figure 5-1 shows the block diagram of a digital optical receiver. It has three sections: 1.Front End 2.Linear Channel and 3.Data recovery. The front end consists of a reverse biased PIN photodetector. The PIN photodetector converts the optical bit stream into an electrical time varying signal. In some cases, the output of the photodetector passes through a pre-amplifier.

The linear channel consists of a high gain amplifier followed by a low pass filter. To limit the average output voltage to fixed level irrespective of the incident optical power, the amplifier gain is controlled automatically using AGC (Automatic Gain Control). The low pass filter is used to truncate the noise spectrum. Since the variance of receiver noise is proportional to the receiver bandwidth, it's desirable to keep the band width of a low pass filter sufficiently low. However, the low pass filter truncates the signal spectrum too. The bandwidth of the low pass filter should be optimized, so

that the SNR is maximized as well. Usually SNR is maximized if the receiver bandwidth is roughly equal to the bit rate.

The Data recovery section consists of a decision circuit and a clock recovery circuit. Suppose the bit pattern at the input end of a fiber-optic link is "1011" as shown in Figure 5-7. Some of these maybe corrupted due to the noise added by the fiber-optic link or by the receiver. Suppose that the peak current at the receiver is 100mA, and the threshold current is 50mA. If the received current is more than 50mA at the sampling time (usually at the middle of the bit interval), the decision circuit interprets it as '1', otherwise the received bit is '0'. In the following figure, the second bit transmitted is '0', but because of the noise, the received current corresponding to that bit is more than the threshold current; therefore, decision circuit interprets it as '1' causing a bit error. The sampling time for the decision is provided by a clock, which is extracted from the received signal using a clock recovery circuit.

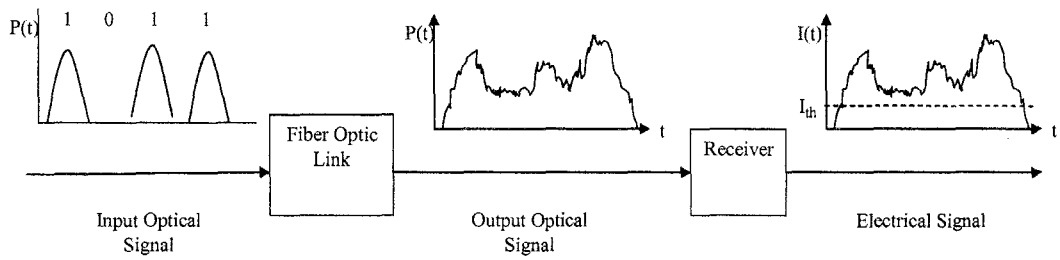


Figure 5-2: The schematic view of fiber-optic link with noise component.

### 5.1.2 Optical Receiver Noise

Optical signal is converted into electrical current by optical receiver. A fraction of electric current generated from optical receiver is from a stream of electrons generated

at random times. This leads to a noisy component in the current. This noisy component is called short noise, and the current due to this noise is called short noise. As the temperature increases, electrons move faster and therefore electrical current increases. However, the mean value of the current is zero, because there are as many electrons moving in one direction as there are in another on the average. Because of the random motion of electrons, the resulting current is noisy and is called thermal noise. The current due to thermal noise is called thermal noise current,

$$I(t) = I_p + I_s(t) + I_T(t) \tag{88}$$

$I_p$ is the deterministic part of the current.
$I_s(t)$ is the noise component of the current due to short noise.
$I_T(t)$ is the noise component of the current due to thermal noise

In order to simplify our study on the optical receiver, we did not take thermal noise into consideration, and also omitted the thermal noise current. After an optical signal of power $P_0$ falls on the photodetector, the current can be written as:

$$I(t) = I_p + I_s(t) \tag{89}$$

$$I_p = RP_0 \tag{90}$$

The short noise current $I_s(t)$ is a random variable with zero mean, $E[I_s(t)] = 0$, and $E$ stands for expectations

The average noise power associated with shot noise is $N_s = E\left[\left(I_s(t)\right)^2\right]R_L = {\sigma_S}^2 R_L$.

Where $\sigma_S$ is the standard deviation and $R_L$ is the load resistor. The signal power (deterministic part) is given by $S = {I_P}^2 R_L = (RP_0)^2 R_L$.

The short noise is a white noise and its power spectral density is constant. It is given by $PSD_S = qI_PR_L$ where $q$ is electron charge.

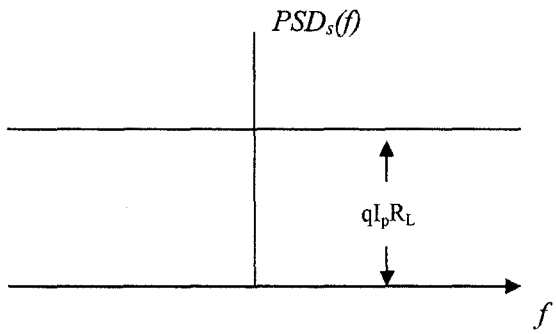


Figure 5-3: The power spectral density of short noise ($PSD_S$).

For simplicity, let us assume that receiver is an ideal low pass filter with one-sided bandwidth $\Delta f$.

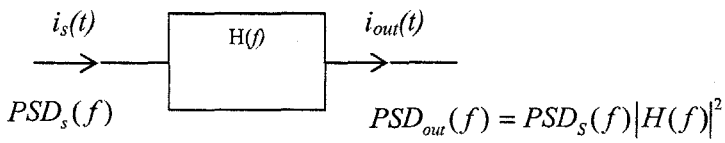


Figure 5-4: The power spectral densities at both input and output end of ideal LPF.

The short noise generated in the photodetector passed through the rest of the receiver circuit. Based on Figure 5-4, the average noise power at the output of the receiver is:

$$N_s = \int_{-\infty}^{+\infty} PSD_{out}(f)df = \int_{-\infty}^{+\infty} PSD_S(f)|H(f)|^2 df \qquad (91)$$

$$= qI_PR_L \int_{-\infty}^{+\infty} |H(f)|^2 df = 2qI_PR_L\Delta f = \sigma_S{}^2 R_L$$

$$\sigma_S^2 = 2qI_P\Delta f \tag{92}$$

### 5.1.3 The Simplified Model for Optical Receiver

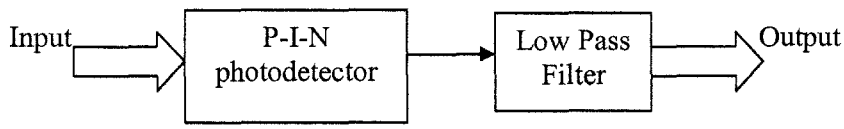


Figure 5-5: The schematic view of simplified optical receiver.

Due to the complexity of theoretical optical receiver, we proposed a simplified version of optical receiver. There are only two components in this simplified structure, one is PIN photodetector, and the other is low pass filter. We have modeled and simulated these devices in the previous chapters respectively. After the optical signal gets amplified by SOA, it goes through the optic fiber and becomes the input of PIN photodetector. Because of the photoelectrical effect of photodetector, the optic signal becomes electrical signal with short noise. After the electrical signal passes through the low pass filter, the high frequency noise in the electrical signal will be dramatically reduced. Since this LPF is not an ideal filter, acceptable delay and certain attenuation is inevitable.

## 5.2 Proposed Saturable Optical Receiver (SOR) for FTTH Network

Even though place repeaters in the system can effectively overcome signal attenuation, optical signal still loses its energy due to other factors, such as fiber absorption, signal dispersion and noise interference. As the transmission distance becomes longer, the signal becomes weaker and more distorted. In order to stabilize the signal strength and increase system efficiency of PON, we coupled a semiconductor optical amplifier (SOA) in front of PIN photodietector, which located at the end users' ONT. An optical filter is generally used to between SOA and receiver to filter out parts of amplified spontaneous emission (ASE) outside the spectrum of optical signal [36]. However, we omitted optical filter in our paper. This is shown in Figure 5-6.

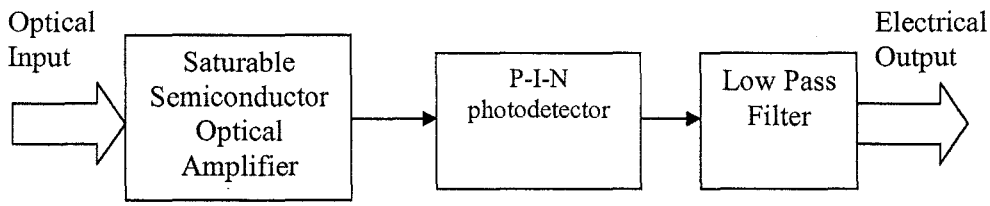


Figure 5-6: The proposed saturable optical receiver (SOR) for FTTH network.

In the real world, tens to a few hundreds of customers may have to share a single fiber-optic transmission system. Because these equipments, such as transmitters and amplifiers, remains too expensive to install all the way to each single home, at least for present services. For Customers located at variable distances from the transmission station, they will receive signals at different strengths, because signal strength is reversibly proportional to the transmission distance. The special gain

property of SOA comes in handy in this case, because the gain of SOA is self-adjusted according to the input optical power. In other words, if the power of input optical signal is too high, the SOA will barely amplify the optical signal; in the contrary, if the power of the input optical signal is too low, the SOA will amplify the input signal instead. After the signal passes through SOA, PIN photodetector converts optical signal into electrical signal through photoelectrical effect. The high frequency noise in the electrical current can be reduced by passing through low pass filter (LPF) afterwards.

## 5.3 Simulation Results

During the simulation, we used randomly generated return-to-zero rectangular waveform. As shown in Figure 5-7, the incident power is 0.1 mW, which approximately correspond to -10 dBm in the horizontal axis of Figure 2-5. The data rate is 1 Gbit/s, and the total time duration is 127 ns. After the optical signal propagates through SOA, the output waveform is shown is Figure 5-8. The output power of SOA is approximately equals to 10 mW.

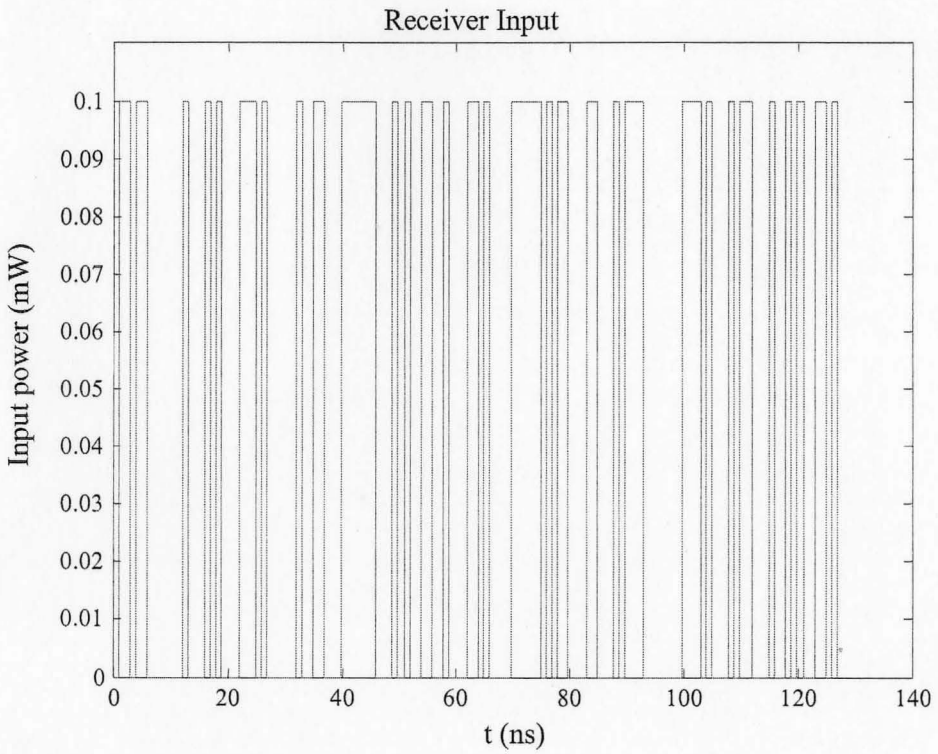


Figure 5-7: The schematic view of return-to-zero input waveform when the incident power equals to 0.1 mW.

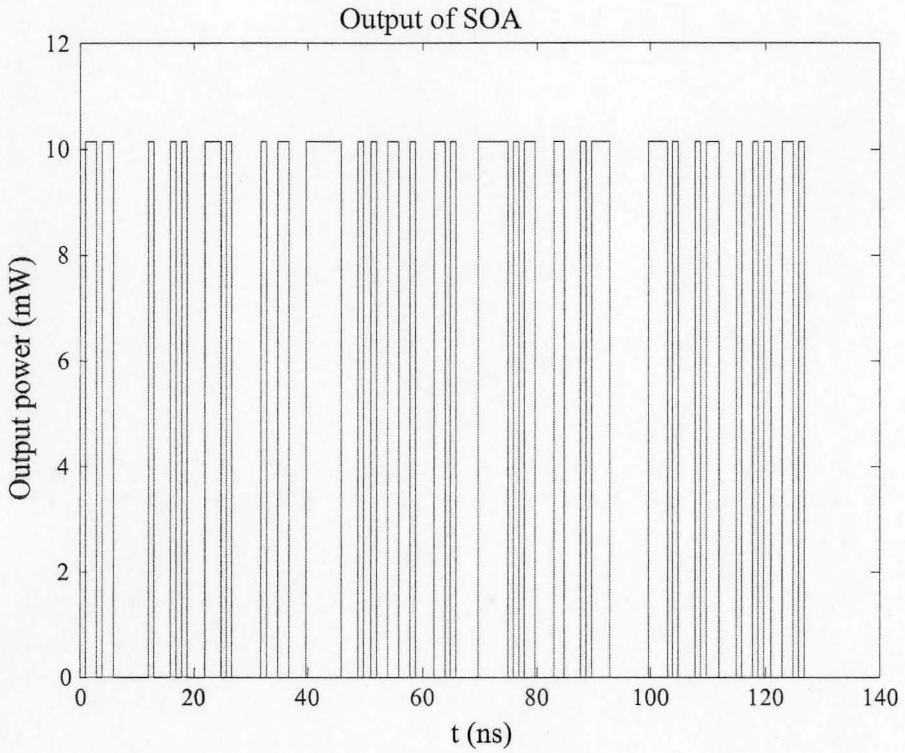


Figure 5-8: The schematic view of return-to-zero output waveform when the incident power equals to 0.1 mW.

After the incident optical signal passes through SOA, as shown in Figure 5-8, the optical signal power will be transformed to current by PIN photodetector through photoelectrical effect. This is shown in Figure 5-9, which includes both deterministic current and short noise current.

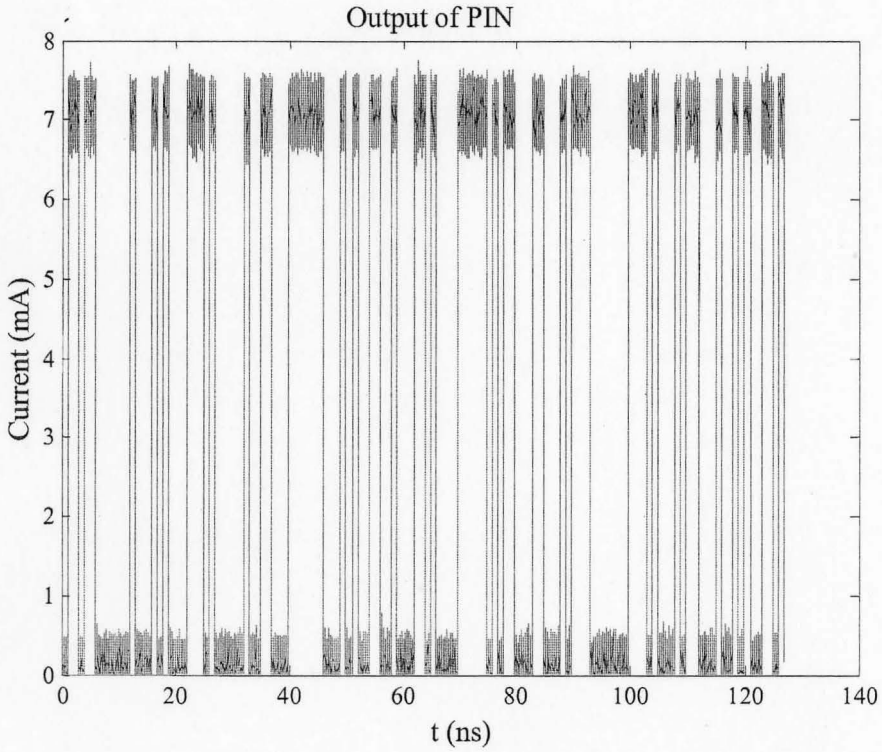


Figure 5-9: The output current from PIN photodetector, when the output power from SOA is 10 mW. This Figure includes both deterministic current and short noise current.

In order to reduce the short noise to the minimum level, as shown in Figure 5-9, we pass the PIN photodetector current through LPF. The output current from LPF is shown in Figure 5-10.

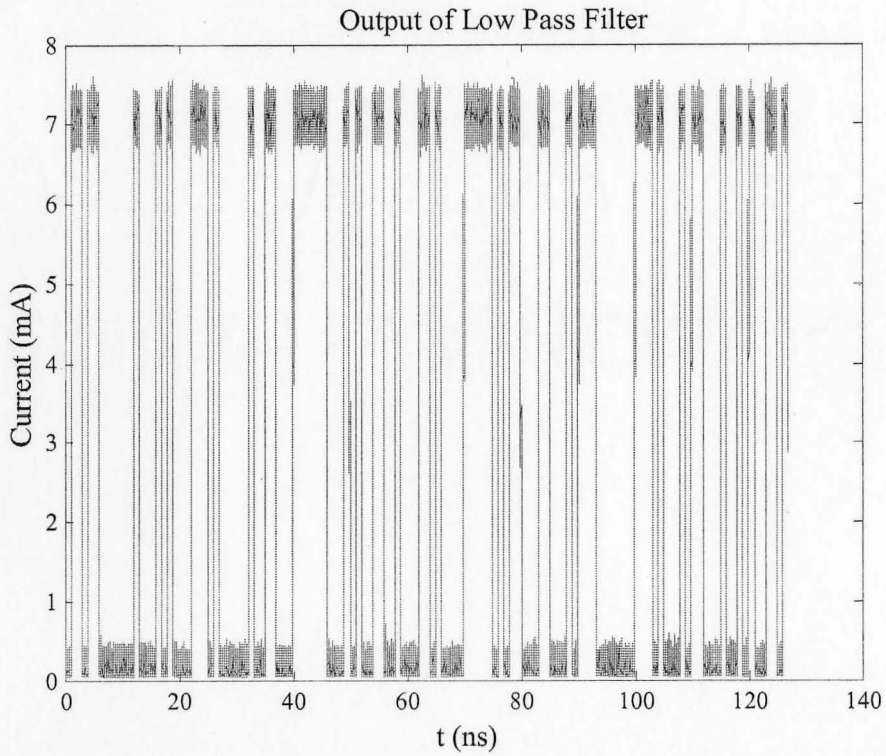


Figure 5-10: The output current from low pass filter, which corresponds to PIN current in the Figure 5-9.

During the second simulation, we set the incident power equals to 1mW, which approximately correspond to 0 dBm in the horizontal axis of Figure 2-5. The data rate is still 1 Gbit/s, and the total time duration is 127 ns. This is shown in Figure 5-11. After the optical signal propagates through SOA, the output waveform is shown is Figure 5-12. The output power is approximately equals to 12 mW. After the photoelectric effect, the PIN current is shown in Figure 5-13. The output current from LPF after noise reduction is shown in Figure 5-14.

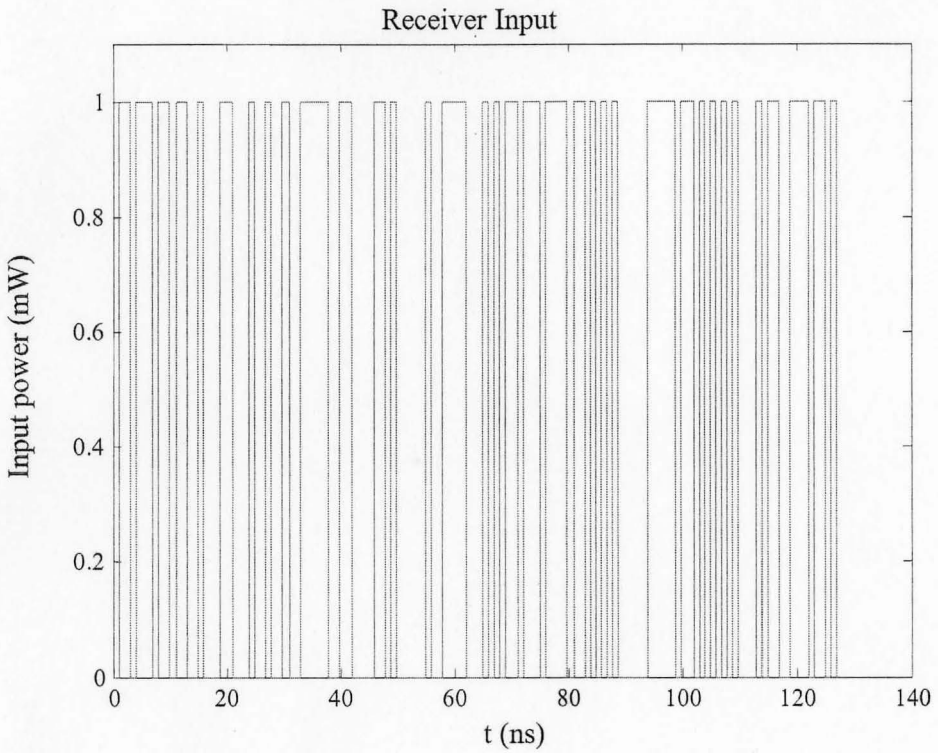


Figure 5-11: The schematic view of return-to-zero input waveform when the incident power equals to 1 mW.

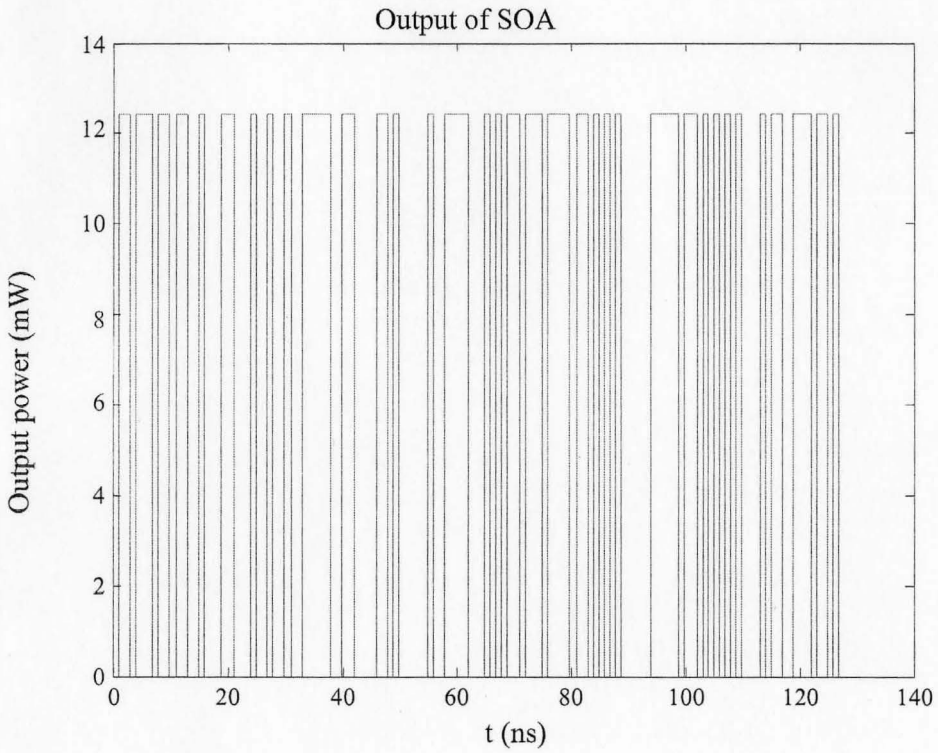


Figure 5-12: The schematic view of return-to-zero output waveform when the incident power equals to 1 mW.

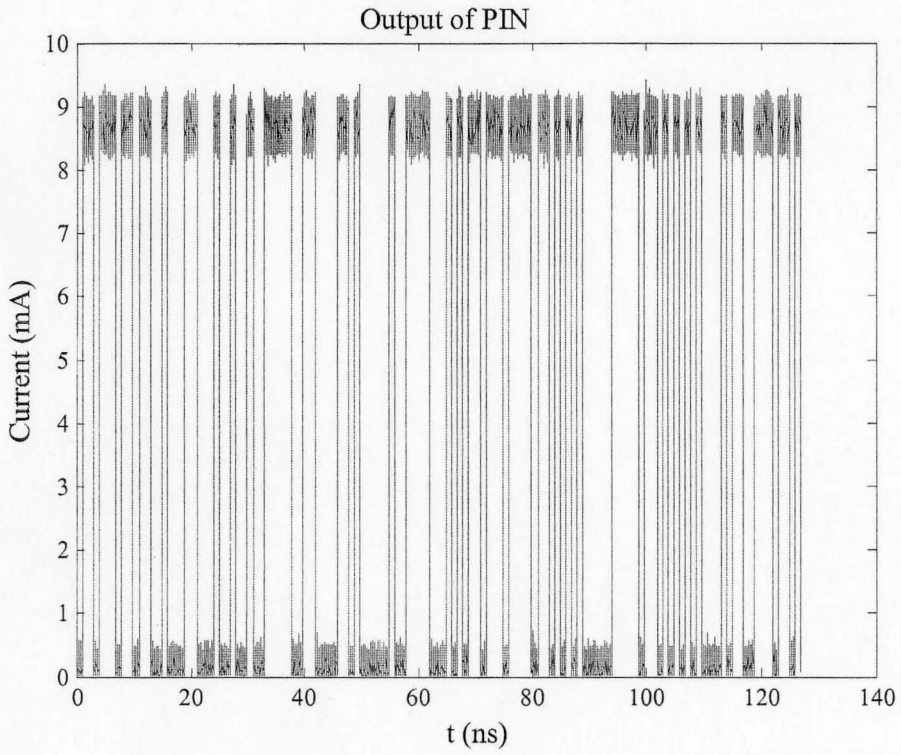


Figure 5-13: The output current from PIN photodetector, when the output power from SOA approximately equals to 12 mW. This figure includes both deterministic current and short noise current.

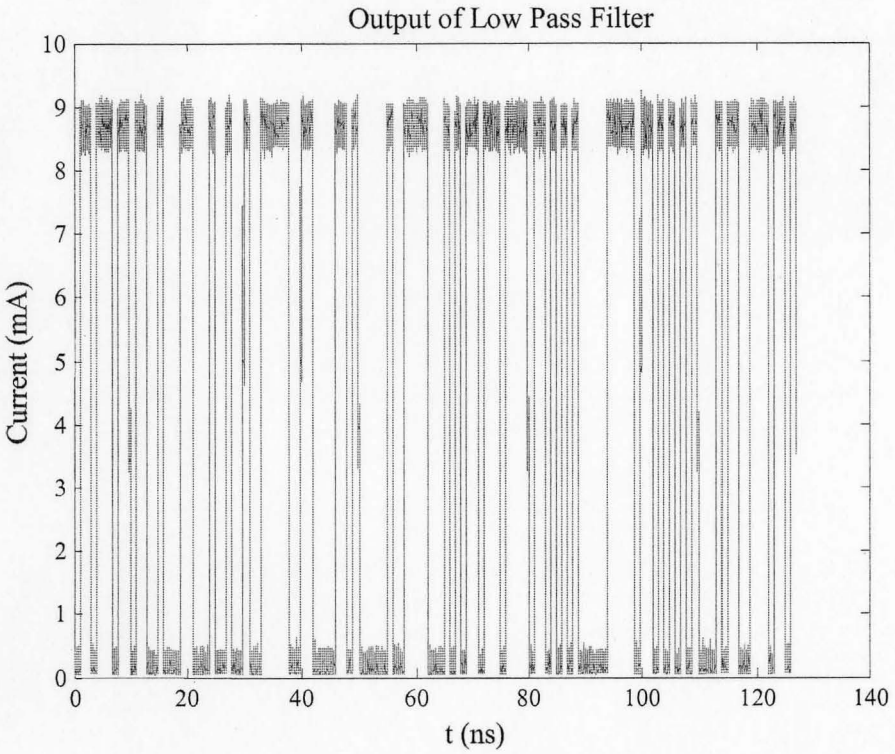


Figure 5-14: The output current from low pass filter, which corresponds to PIN current in the Figure 5-13.

## 5.4 Comparisons

In Chapter 2, we simulated SOA when the input powers are 3.163 mW and 0.3163 mW. The results were shown in Figure 2-7 and Figure 2-9 respectively. In this Chapter, when the input powers of SOA are 0.1 mW and 1 mW, the output powers from SOA are shown in Figure 5-8 and Figure 5-12 respectively. In order to make better illustration of SOA's gain property, we summarized these results as following:

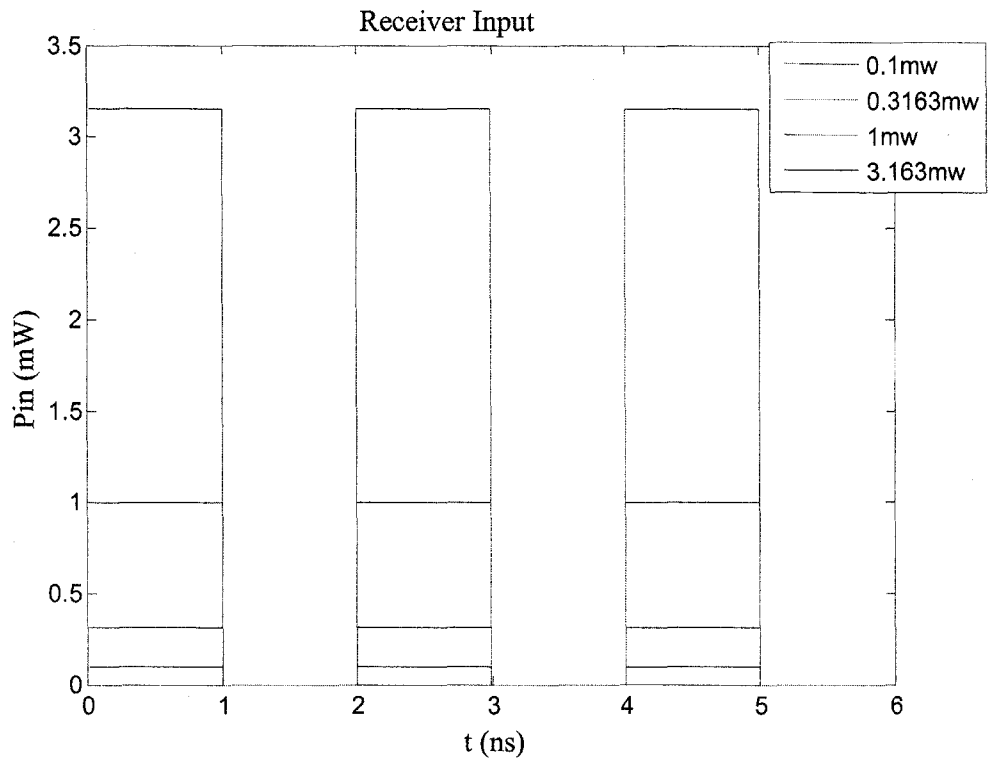


Figure 5-15: The schematic view of different input powers of SOA.

Even though the inputs powers of SOA are significantly different from each other, the output powers are almost non-changed. This is shown in Figure 5-16.

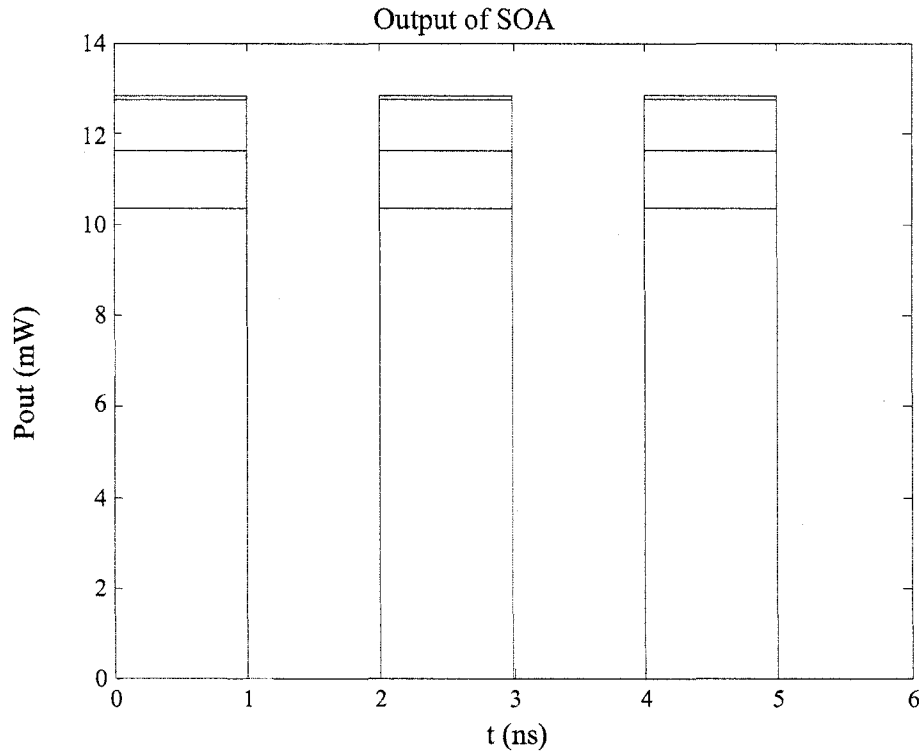


Figure 5-16: The schematic view of different output powers of SOA, which are correspond to Figure 5-15.

The incident power 3.163 mW is thirty times bigger than 0.1 mW at the input of SOA; however, based on the Figure 5-16, the maximum difference between output powers are 0.003 mW, which is certainly negligible. This gain property of SOA can be utilized at the receiver end of FTTH network, which would definitely increase the stability of optical signals at subscribers' optical network terminal (OPT).

# Chapter 6 Conclusion and Future Work

Numerical models considering the interaction among the carriers, the multichannel optical signal fields and the spontaneous emission noise in the SOA are necessary for accurate description of the underlying physics for the operation of such devices [14]. In this respect, the time-domain traveling wave models have been applied and validated in the modeling and simulation of SOA [14]. Different from the laser diodes (LDs) that operate in a narrow spectral range, the SOAs have to be described in a broad wavelength band as the multi-channel signals may spread over the entire gain spectrum where spontaneous noise is also emitted and coupled into the signal [14]. For this purpose, a comprehensive model is developed in a self-consistent fashion. By solving the broad-band time-domain traveling wave model, we examined the performance of typical SOAs with respect to a variety of operation and design parameters [14]. In our model, the spontaneous emission noise was generated by random sources over the entire spectrum and is coupled to the signal channels in a self-consistent manner [14]. Our model also incorporated the gain dynamics as the material gain is updated at each time step [14]. This would be necessary since the carrier density changes locally therefore make the gain changes at each time step, and this, in turn, affects the spontaneous noise generation [14].

In order to solving this broad-band time-domain traveling wave model efficiently, we have described 13 essential steps of the deviation of an efficient numerical solver of SOAs. Although the described numerical solver gives an accurate description of the device, including propagation effects especially important when SOAs operate under saturation, it does not require long computational times, because it is based on the solution of a set of ordinary differential equations [27]. Furthermore, since the

device description is based on input-output relations, the simulator is ready to be inserted into more general modular simulators of optical transmission systems [27]. These features make the numerical model developed a useful tool for the optimization and evaluation of the performance of SOAs inserted into a real transmission systems [27].

There are several different architectures for the implementation of FTTH network. The architecture of FTTH network we used in our paper is called Home Run Fiber, and is shown in Figure 6-1. It has a dedicated fiber that is deployed all the way from the central transmission station to each subscriber premise [1]. In addition, this architecture requires one ONT port per home.

In the Home Run Fiber, multiple users located at variable distances from the central transmission station, the signals will reach users at variable strengths. If a user locates very close to the transmission station, the signal will be too strong for the user, and cause unnecessary bandwidth waste. On the other hand, the user located far away from the transmitter will receive weaker and more distorted signal. This is shown in the Figure 6-1. I.e. user 1 locates further from the station than user 2. Since both output signals come from the same transmission station, they approximately have the same signal strengths when they leave the station. However, after both signals pass through optical fibers and get to their designated users respectively, output signal 1 will become much weaker and distorted than output signal 2.

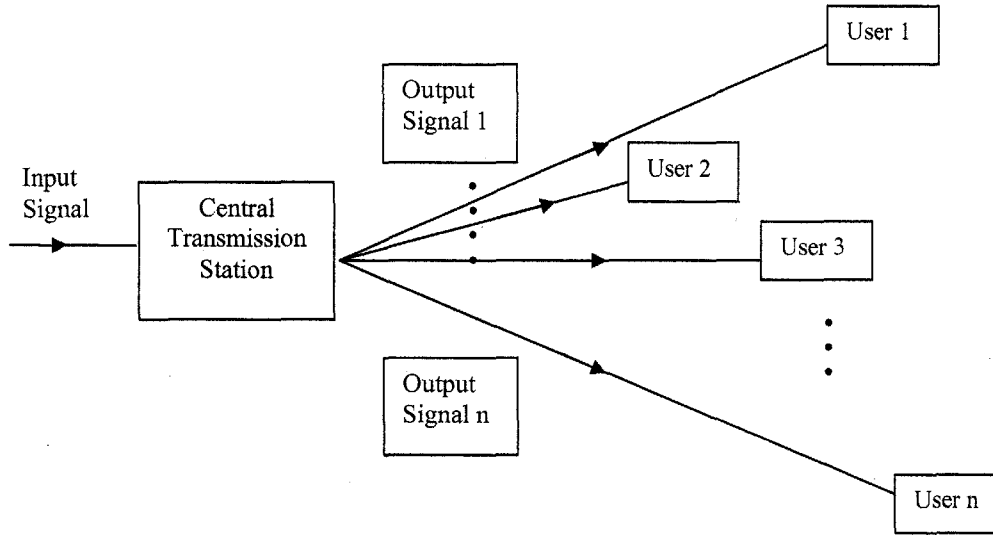


Figure 6-1: Simplified schematic diagram of FTTH network.

The signal stability of the FTTH network at the customer premises has been largely limited by the above drawback. We proposed an effective solution for this issue with detailed simulation. The proposed solution is that we can couple a SOA directly with PIN photodetector at each ONT (subscriber node). When the weakened and distorted signal reaches the ONT, the SOA amplifies the optical signal first. Before the optical signals can be properly accepted by the customers, they have to be converted back to the electrical currents by passing through PIN photodetector. Since high frequency noise component have already mixed into the signals during the transmission, the converted currents have to pass through a LPF in order to keep the effect of noise at a minimum level.

In reality, people around the world have quickly recognized the beneficial of FTTH technology as they look to next-generation networks for faster internet and more robust video services. Globally, 2007 was the best year yet in terms of numbers

of new subscribers to FTTH services, where a total of nearly 6 million new FTTH households were added [37]. The distribution of FTTH networks around the world is shown in Figure 6-2: [37]

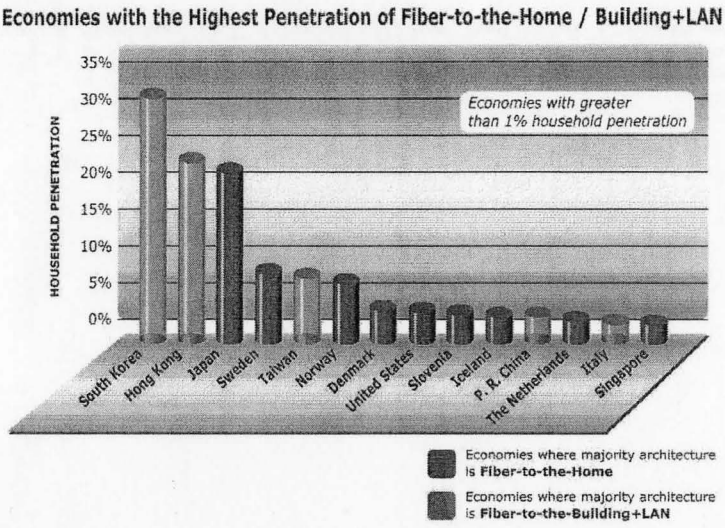


Figure 6-2: Countries where more than one percent of households are connected directly into high speed fiber optic networks.

Although the number of countries where fiber to the home connections are showing significant gains in the broadband services market continues to expand, A number of difficulties in this application still have to be overcome. In our paper, we only proposed one possible solution for the enhancement of signal stability at the ONT. Other drawbacks, such as high cost for construction and low system reliability between premises and indoor lines, are still up against higher market distribution.

FTTH as a newly developed technology is still in the distribution process, it has been matured in both technical and economical aspects during the past several years [1]. The consumer benefits of FTTH continue to be so significant and the

technological innovations are so impressive that they are a vital element of our broadband future [37].

# Bibliography

[1] Luo, R., Ning, T. G., Li, T. G., Cai, L. B., Qiu, F., Jian, S. S., & Xu, J. J. (2005). *FTTH-A Promising Broadband Technology*. Paper presented at Communications, Circuits and Systems Proceedings International Conference (*pp. 609-612*).

[2] Huang, W. P., Li, X., Xu, C. Q., Hong, X., Xu, C. L., & Liang, W. (2007), Optical Transceivers for Fiber-to-the-Premises Applications: System Requirements and Enabling Technologies. *J. Lightwave Technology, 25(1)*, pp 11-27.

[3] Kuramoto, I., Terao, Y., & Honda, H. (2005). *Increasing FTTH Reliability between Premise and Indoor Lines.* Paper presented at Optical Fiber Communication Conference 2005 Technical Digest, Anaheim, CA.

[4] Agrawal, G. (1997). *Fiber –optic Communication Systems (2nd ed.)*. New York, NY: Wiley.

[5] Kumar, S. (2007), *ECE.756 Course Notes: Design of Lightwave Communication Systems and Networks*, Retrieved April 2007, from *McMaster University, Department of Electrical and Computer Engineering* Web site: http://www.ece.mcmaster.ca/~kumars/Photon_dev.htm.

[6] Connelly, M. J. (2002*). Semiconductor Optical Amplifiers*. Norwell, MA: Kluwer Academic Publishers.

[7] Schneider, K. S. *Telebyte Fiber Tutorial Notes: Fiber Optic Communications for the Premises Environment,* Retrieved 2003, from *Telebyte* Web site: http://www.telebyteusa.com/foprimer/foprimer.htm.

[8] Castelli, R., & Krause, T. (1998). Market trends and evolution for optical transmission systems. *Alcatel Telecommun. Rev.,* pp 165-175.

[9] Chan, V. W. S., Hall, K. L., Modiano, E., & Rauschenbach, K. A. (1998). Architectures and technologies for high-speed optical data networks. *J. Lightwave Technology., 16*, 2146–2168.

[10] Iannone, E., & Sabella, R. (1996). Optical path technologies: A comparison among different cross-connect architectures. *J. Lightwave Technology, 14*, pp 2184–2196.

[11] Wang, D. X. (2006). *Optical modeling for semiconductor optical amplifiers and solid state lighting.* Unpublished doctoral dissertation, Georgia Institute of Technology, Atlanta.

[12] Connelly, M. (2002). *Semiconductor Optical Amplifiers and their Applications.* Unpublished doctoral dissertation, University of Limerick, Ireland.

[13] Park, J., Li, X., & Huang, W. (2003). Performance Simulation and Design Optimization of Gain-Clamped Semiconductor Optical Amplifiers Based on Distributed Bragg Reflectors. *IEEE J. Quantum Electronics, 39*, pp 1415-1423.

[14] Stubkjaer, K. E. (2000). *Semiconductor optical amplifier-based all-optical gates forhigh-speed optical processing. IEEE J. Sel. Top. Quantum Electron., 6 (6)*, pp 1428-1435.

[15] Mecozzi, A., & Wiesenfeld, J. (2001). The roles of semiconductor optical amplifiers in optical networks. *Opt. & Photon News, 12*, pp 36-42.

[16] Marcuse, D. (1983). Computer Model of an injection laser amplifier. *IEEE J. Quantum Electron., 19*, pp 63-73.

[17] Lee, T., Burrus, C., Copeland, J., Dentai, A., & Marcuse, D. (1982). Short-cavity InGaAsP injection lasers: Dependence of mode spectra and single-longitudinal-mode power on cavity length. *IEEE J. Quantum Electron., QE-18*, pp 1101-1113.

[18] Obermann, K., Kindt, S., Breuer, D., & Petermann, K. (1998). Performance analysis of wavelength converters based on cross-gain modulation in semiconductor optical amplifiers. *J. of Lightwave Technol., 16*, pp 78-85.

[19] O'Mahony, M. (1988). Semiconductor laser optical amplifiers for use in future fiber systems. *J. of Lightwave Technol., 6*, pp 531-544.

[20] Li, X., & Park, J. (2006). Time-domain simulation of channel crosstalk and inter-modulation distortion in gain-clamped semiconductor optical amplifiers. *Optical Communications., 263,* pp 219-228.

[21] Gehrig, E., Hess, O., & Wallenstein, R. (1999). *Modeling of the performance of high-power diode amplifier systemswith an optothermal microscopic spatio-temporal theory. IEEE J. Quantum Electron., 35 (3),* pp 320-331.

[22] Press, W. H., Flannery, B. P., Teukolssy, S. A., & Vetterling, W. T. (1986). *Numerical Recipes: The art of Scientific Computing.* Cambridge, MA: Cambridge Univ. Press.

[23] Zhang, L. M., Yu, S. F., Nowell, M. C., Marcenac, D., Carroll, J. E., & Plumb, R. G. S. (1994). Dynamic analysis of radiation and side-mode suppression in a second-order DFB laser using time-domain large-signal traveling wave model. *IEEE J. Quantum Electron., 30*, pp 1389–1395.

[24] Li, W., Huang, W. P., Li, X., & Hong, J. (2000). Multiwavelength gain-coupled DFB laser cascade: Design modeling and simulation. *IEEE J. Quantum Electron., 36,* pp 1110–1116.

[25] Hinton, K. (1989). A model for noise processes in semiconductor laser amplifiers, part 1: the traveling-wave semiconductor laser amplifier. *Opt. Quantum Electron., 21,* pp 33–46.

[26] Park, J., Li, X., & Huang, W. P. (2005). Comparative study of mixed frequency-time-domain models of semiconductor laser optical amplifiers. *IEE Proc.-Optoelectron., 152(3),* pp 151-159.

[27] Cassioli, D., Scotti, S., & Mecozzi, A. (2000). A Time-domain Computer Simulator of the Nonlinear Response of Semiconductor Optical Amplifiers. *IEEE J. Quantum Electronic., 36(9),* pp 1072-1080.

[28] Yang, K., *Gutierrez-Aitken, A.L., Zhang, X., Haddad, G.I., & Bhattacharya, P.* (1996). Design, modeling, and characterization of monolithically integrated InP-based (1.55 um) high-speed (24 Gb/s) p-i-n/HBT front-end photoreceivers. *J. Lightwave Technology., 14(8),* pp 1831 – 1839.

[29] Jaeger, R. C. (2004). *Microelectronic Circuit Design (2nd ed.).* Canada: McGraw-Hill.

[30] Rodríguez, D. (2004). *MATLAB Exercise Dar_a6 – Digital Signal Processing.* Retrieved June13, 2008, from *University of Puerto Rico* Web site: http://www.ece.uprm.edu/~domingo/teaching/inel5309/DAR_A6_MATLAB.doc.

[31] Li, X. (2000). *Group Internal Report: LPF Realization in Time-Domain through IIR-DSP*, Retrieved March 2008, from *McMaster University, Department of Electrical and Computer Engineering.*

[32] Nocedal, J., & Wright, S. J. (1999*). Numerical Optimization.* New York, NY: Springer.

[33] Mathematic and Computer Science Division, Argonne National Laboratory.(n.d.). *Optimization. Software Guide of NEOS.* Retrieved from: http://www.mcs.anl.gov/otc/Guide/SoftwareGuide

[34] Dennis, J. E., Gay, D.M., & Welsch, R.E. (1981). An Adaptive Nonlinear Least-Squares Algorithm. *ACM Trans Math Softw. 7(3),* pp 348-368.

[35] Haykin, S. (2000). *Communication Systems (4th ed.).* New York, NY: Wiley.

[36] Caplan, D.O. (2007). Laser communication transmitter and receiver design. *J. Opt. Fiber Commun. Rep., 4(4-5),* pp 225-362.

[37] Manning, J., & Evans, D. (2008). Fiber to the Home Deployment Spreads Globally As More Economies Show Market Growth. *Fiber to The Home Council., 1*, pp 5-8.

[38] Yamada, E., Suzuki, K., & Nakazama, M. (1991). *Electron. Lett., 27*, pp1289.

[39] Nakazawa, M., Yamada, E., Kuobota, H., & Suzuki, K. (1991). *Electron. Lett., 27*, pp1270.

[40] Gordon, J. P., & Haus, H. A. (1986). *Opt. Lett., 11*, pp665.

[41] Tajima, K. (1987). *Opt. Lett., 12*, pp54.

[42] Kruskal, M. D., & Zabusky, N. (1965). *Phys. Rev. Lett., 15*, pp240.

[43] Tappert, F., & Hasegawa, A. (1973). *Appl. Phys. Lett., 23*, pp142.

[44] Zhao, W., & Bourkoff, E. (1990). *Opt. Lett., 15*, pp405.

[45] Doran, N. J., & Blow, K. J. (1985). *Phys. Lett., 107A*, pp55.

[46] Kivsar, Yu. S. (1990). *Phys. Rev., A42*, pp1757.

[47] Tajima, K. (1987). *Opt. Lett., 8*, pp650.

[48] Mollenauer, L. F., Neubelt, M. J., Evangelides, S. G., Gordon. J. P., Simpson, J. R., & Cohen, L. G. (1990). *Opt. Lett., 15*, pp1203.

[49] Iwatasuki, K., Takada, A., Nishi, S., & Saruwatari, M. (1989). *Electron. Lett., 25*, pp1003.

[50] Mollenauer, L. F., Neubelt, M. J., Lichtman, E., Evangelides, S. G., & Nyman, B. M. (1991). *Electron. Lett., 27*, pp2055.

[51] Wood, J. (1995). *J. Opt. Soc. Am., B8*, pp1097.

[52] Lisak, M., & Anderson, D. (1996). *Phys. Rev., A32*, pp2270.

[53] Chirkin, A. S., & Fattakhov, A. M. (1994). *Sov. J. Quantum Electron., 14*, pp1556.

[54] Simpson, J. R., Shang, H. T., Mollenauer, L. F., Olsson, N. A., Becker, K. S., Lemaire, P. J., & Neubelt, M. J. (1991). *J. Lightwave Technol., 9*, pp228.

[55] Simpson, J. R., Logan, R. A., Olsson, N. A., Tanbun-Ek, T., Andrekson, P. A., Becker, P. C., & Wecht, K. W. (1990). *Electron. Lett., 26*, pp1499.